JMB

Ions and Counterions in a Biological Channel: A Molecular Dynamics Simulation of OmpF Porin from *Escherichia coli* in an Explicit Membrane with 1 M KCl Aqueous Salt Solution

Wonpil Im and Benoît Roux*

Department of Biochemistry Weill Medical College of Cornell University, 1300 York Avenue, New York, NY 10021 USA

A 5 ns all-atom molecular dynamics trajectory of *Escherichia coli* OmpF porin embedded in an explicit dimyristoyl-phosphatidylcholine (DMPC) bilayer bathed by a 1 M [KCl] aqueous salt solution is generated to explore the microscopic details of the mechanism of ion permeation. The atomic model includes the OmpF trimer, 124 DMPC, 13470 water molecules as well as 231 K^+ and 201 Cl^-, for a total of 70,693 atoms. The structural and dynamical results are in excellent agreement with the X-ray data. The global root-mean-square deviation of the backbone atoms relative to the X-ray structure is 1.4 Å. A cluster of three fully charged arginine (Arg42, Arg82, and Arg132) facing two acidic residues (Asp113 and Glu117) on L3 in the narrowest part of the aqueous pore is observed to be very stable in the crystallographic conformation. In this region of the pore, the water molecules are markedly oriented perpendicular to the channel axis due to the strong transversal electrostatic field arising from those residues. On average the size of the pore is smaller during the simulation than in the X-ray structure, undergoing small fluctuations. No large movements of loop L3 leading to a gating of the pore are observed. Remarkably, it is observed that K^+ and Cl^- follow two well-separated average pathways spanning over nearly 40 Å along the axis of the pore. In the center of the monomer, the two screw-like pathways have a left-handed twist, undergoing a counter-clockwise rotation of 180° from the extracellular vestibule to the pore periplasmic side. In the pore, the dynamical diffusion constants of the ions are reduced by about 50% relative to their value in bulk solvent. Analysis of ion solvation across the channel reveals that the contributions from the water and the protein are complementary, keeping the total solvation number of both ions nearly constant. Unsurprisingly, K^+ have a higher propensity to occupy the aqueous pore than Cl^-, consistent with the cation selectivity of the channel. However, further analysis suggests that ion–ion pairs play an important role. In particular, it is observed that the passage of Cl^- occurs only in the presence of K^+ counterions, and isolated K^+ can move through the channel and permeate on their own. The presence of K^+ in the pore screens the negative electrostatic potential arising from OmpF to help the translocation of Cl^- by formation of ion pairs.

Corresponding author   *Keywords:* permeation; diffusion; ion solvation; ion pairing; β-barrel

Present address: W. Im, Department of Molecular Biology (TPC6), The Scripps Research Institute, 10550 North Torrey Pines Rd, La Jolla, CA 92037, USA.

E-mail address of the corresponding author: Benoit.Roux@med.cornell.edu

Introduction

The outer membrane of *Escherichia coli* protects the cell against hostile agents and facilitates the uptake of nutrients. This activity is mediated by macromolecular structures called porins.[1–3] These nonspecific porins, which allow the diffusion of hydrophilic molecules with molecular mass up to

600 Da, are not very selective and have only some specificity toward cations or anions. While the cation-selective matrixporin (OmpF), a major component of the outer membrane of *E. coli*, is produced under normal conditions, the anion-selective phosphoporin (PhoE) and the cation-selective osmoporin (OmpC) are expressed under phosphate limitations or under conditions of osmotic stress, respectively.

The three-dimensional structure of several porins has been determined to high resolution by X-ray crystallography.[4–9] For general reviews on porins the reader is referred to Schulz,[10] Schirmer,[11] and Koebnik *et al.*[12] The porins have a high degree of sequence similarity, about 71% for OmpF, PhoE and OmpC. OmpK36 of *Klebsiella pneumoniae* is a closely related homologue of osmoporin (OmpC) of *E. coli*, with 81% identity. Most of the porins fold into similar homo-trimeric structures. Each monomer consists of a 16-stranded β-barrel with eight short turns (T1–T8) at the periplasmic side and eight relatively large loops (L1–L8) at the cell surface which confers a significant stability and rigidity to the structure. Each monomer possesses a wide aqueous pore narrowed by the loops on the outer entrance of the β-barrel. One of these loops (L3) is folded inside the β-barrel forming a narrow region of about 6 Å diameter within the wide aqueous channel at roughly half-way through the membrane. This narrowest region of the pore, called the "constriction zone", is thought to be responsible for the charge specificity of the porins. For example, the structural basis for the difference in selectivity of OmpF for cations and PhoE for anions has been attributed to the presence of a lysine in PhoE in the constriction zone, substituting for a glycine in OmpF.[5]

The permeation properties of the bacterial porins are generally characterized with KCl or NaCl salt solutions over a wide range of concentration (from 5 mM to 3 M),[1,8,13–16] although it is very difficult to have stable experimental conditions under 50 mM salt solutions and those measurements have a higher uncertainty (N. Saint, personal communication). The single-channel conductance and the cation–anion permeability ratio P_c/P_a of OmpF, PhoE, and various OmpF mutants,[14–16] *Rhodobacter capsulatus* porin,[1] and OmpK36 of *K. pneumoniae* (homologous to OmpC)[8] have been measured mostly in NaCl solutions. The single-channel conductance in 1 M KCl salt solution is about 1.9 nS for OmpF, 1.8 nS for PhoE, and 1.5 for OmpC,[13] although recent measurements indicate that the conductance of OmpF in 1 M KCl is around 1.45 nS[17] or 1.34 nS (N. Saint, personal communication). The permeability ratio P_c/P_a was determined from the reversal potential with a tenfold KCl concentration gradient (10 mM and 100 mM); it is about 3.8 for OmpF, 0.30 for PhoE, and 26 for OmpC.[13] The dependence of the single-channel conductance on salt concentration is normally attributed to variations in charge screening by the salt at the pore mouth.[18] It should be noted that porins do not act simply as passive pores, but can also exhibit some complex voltage-dependent gating activity. The probability of opening and closing transitions of the pores, observed in single-channel experiments, depends on the applied transmembrane potential.[19] The microscopic origin of this observed behavior is, however, poorly understood. Cross-linking experiments have shown that movements of L3, initially proposed to be responsible for closing of the pors,[20–22] are not required for voltage-gating.[19,23] Atomic force microscopy (AFM) imaging has revealed the possibility of alternate structural conformation on the outer surface of the channel which could be responsible for the voltage-gating.[24,25]

Because they are well characterized, both structurally and functionally, the porins represent ideal systems for addressing questions about the fundamental principles underlying ion flow in molecular pores at the molecular level using theoretical models. There have been a number of theoretical studies of porins, focusing on different aspects of porin activity. Schirmer and co-workers have used the Poisson–Boltzmann (PB) equation to determine the ionization state of titratable residues and explore the nature of electrostatic fields in OmpF and PhoE.[26,27] In particular, it was noted that a cluster of three arginines (Arg42, Arg82, and Arg132) facing two acidic residues (Glu117 and Asp113) in the constriction zone created an unusually strong transverse electric field perpendicular to the pore axis. From those PB calculations, it was initially inferred that the cluster of three arginines should only carry a total charge of +2e, and would be otherwise unstable and inconsistent with the crystallographic structure. But this conclusion was later revised on the basis of further experimental data by Schirmer & Phale,[15] illustrating some of the limitations of PB calculations in which the protein is generally rigidly fixed and not allowed to relax. The importance of protein flexibility is addressed more readily with molecular dynamics (MD) simulations.[28] MD trajectories have been generated to explore the fluctuations of porins.[20–22,29,30] The influence of the solvent molecules was incorporated implicitly in the early studies,[20–22] and they are inevitably limited for this reason. The later simulations of porins are much more realistic because they were carried out with explicit ions, solvent molecules[29] and also phospholipid bilayer membrane.[30] To explore the mechanism of ion conduction, Suenaga *et al.* simulated OmpF in the presence of an applied transmembrane potential.[29] The translocation of a single Na$^+$ through the channel was observed in 1.3 ns under the influence of a potential of 500 mV. Tieleman & Berendsen generated a 1 ns MD simulation of an atomic model of OmpF trimer embedded into an explicit phospholipid bilayer membrane (for a total of 65,898 atoms).[30] This monumental simulation provided a wealth of information about the solvation of porin and its interaction with the surrounding lipids. However, only a few counterions were

explicitly included (those needed to balance the total charge of OmpF), and therefore little insight could be gained about the ion permeation mechanism.

These previous studies illustrate well the general difficulties in studying ion channels based on all-atom MD simulations with explicit ions and solvent molecules. The calculations are computationally intensive, and yet, the time-scale of ion permeation is significantly longer than can be currently simulated. To avoid these limitations, a number of studies have used Brownian dynamics (BD) to explore the ion conduction mechanism.[15,16,31,32] In this approach, the channel and the ions are represented explicitly while the influence of the surrounding solvent molecules is incorporated implicitly *via* a stochastic random force, a friction coefficient damping the velocity, and some effective potential (generally calculated on the basis of a continuum electrostatic approximation). Schirmer and co-worker generated stochastic trajectories of isolated ions using the program UHBD[33,34] to examine the cation/anion specificity of OmpF, PhoE and OmpK36, as well as several OmpF mutants.[15,16] Only one ion was considered at a time in those simulations and finite-concentration effects were modeled implicitly *via* a PB approximation. A good correlation was achieved between calculated single-ion transmission probabilities and experimental ion selectivity. More recently, Im *et al.* generated BD trajectories of OmpF with explicit multiple ions using a Grand Canonical Monte Carlo (GCMC) and BD algorithm.[31,32] Assuming buﬁlk-like values for the diffusion constant of K^+ and Cl^- in the pore the conductance of OmpF calculated from GCMC/BD simulations with a 200 mM KCl concentration was 420 pS,[32] in relatively good agreement with the experimental estimate of 350 pS (N. Saint, personal communication).

Although much progress has been made to better understand the ion-conducting properties of porins, the current view has been developed, in large part, on the basis of BD simulations and continuum electrostatic PB calculations in which the solvent was represented implicitly. Such approximations are attractive because they are less computationally intensive than all-atom MD. However, their validity is still unknown in the context of molecular pores. For example, the orientational freedom of water molecules has been shown to be considerably affected in the pore[30] and it is unclear whether a structureless dielectric continuum is a valid representation. Furthermore, the channel structure is generally kept rigidly fixed during BD simulations and the coupling to protein fluctuations is ignored. In principle, detailed all-atom MD simulations with explicit ions, solvent and membrane lipids avoid such gross approximations and can provide information that can considerably enhance our understanding of the function of porins at the microscopic level. But as discussed above, the approach is facing significant challenges because it is difficult to obtain statistically meaningful results with finite length simulations due to the relatively small number of ions included explicitly in the simulations.[29,30]

Although the previous PB, BD, and MD studies provided many of the essential elements for understanding the function of outer membrane porins, several fundamental questions still need to be clearly and correctly answered at this point. What is the magnitude of protein fluctuations and what is their influence on the geometry and the size of the narrow pore? Is the charge specificity of OmpF arising only from the residues in the constriction zone, or are more residues being implicated? What are the dominant interactions governing ion translocation at the microscopic level? How is ion diffusion affected and what is the importance of cation–anion pairing in the wide aqueous pore? What are the properties of the water molecules in such confined environment? To address those questions, we have constructed an all-atom model of OmpF embedded in a fully solvated phospholipid bilayer membrane bathed by a 1 M KCl aqueous salt solution and generated a 5 ns MD trajectory. For comparison, a 1 M KCl bulk aqueous solution and a neat DMPC membrane bathed with the same salt solution were also simulated. From a computational point of view, the high salt concentration is advantageous. The large number of ions included explicitly in the simulations significantly helps to obtain statistically meaningful averages of the ion properties in the pore from a trajectory of finite length. A prohibitively long simulation time would be required to obtain convergence by simulating the corresponding atomic model with a low salt concentration. The previous MD simulations included only a small number of explicit ions. Suenaga *et al.* positioned counterions near every charged amino acid residues of OmpF for a total of 41 Na^+ and 25 Cl^-,[29] while Tieleman & Berendsen included only 27 Na^+ to balance the total charge of OmpF.[30] Such treatments of the ions cannot simulate the influence of a finite salt concentration realistically. In comparison, the present simulation of OmpF includes 231 K^+ and 201 Cl^-. It should be stressed, however, that a 1 M KCl salt solution is not unrealistic. Similar salt concentrations are routinely used in experiments to measure ion fluxes[13–16] and in AFM imaging.[35] Interestingly, exposure of *E. coli* to such high salt concentration triggers the expression of OmpC, an outer membrane porin which is more strongly cation selective than OmpF.

The atomic model and the MD simulation protocol are described in the next section. Then, the main observations are described and discussed. Several properties are examined in detail such as the dynamics of the pore and the properties of water and ions inside the channel. A particular attention is given to the average of the ion properties for ion translocation across the aqueous pore. The paper is concluded with a brief summary of the main results.
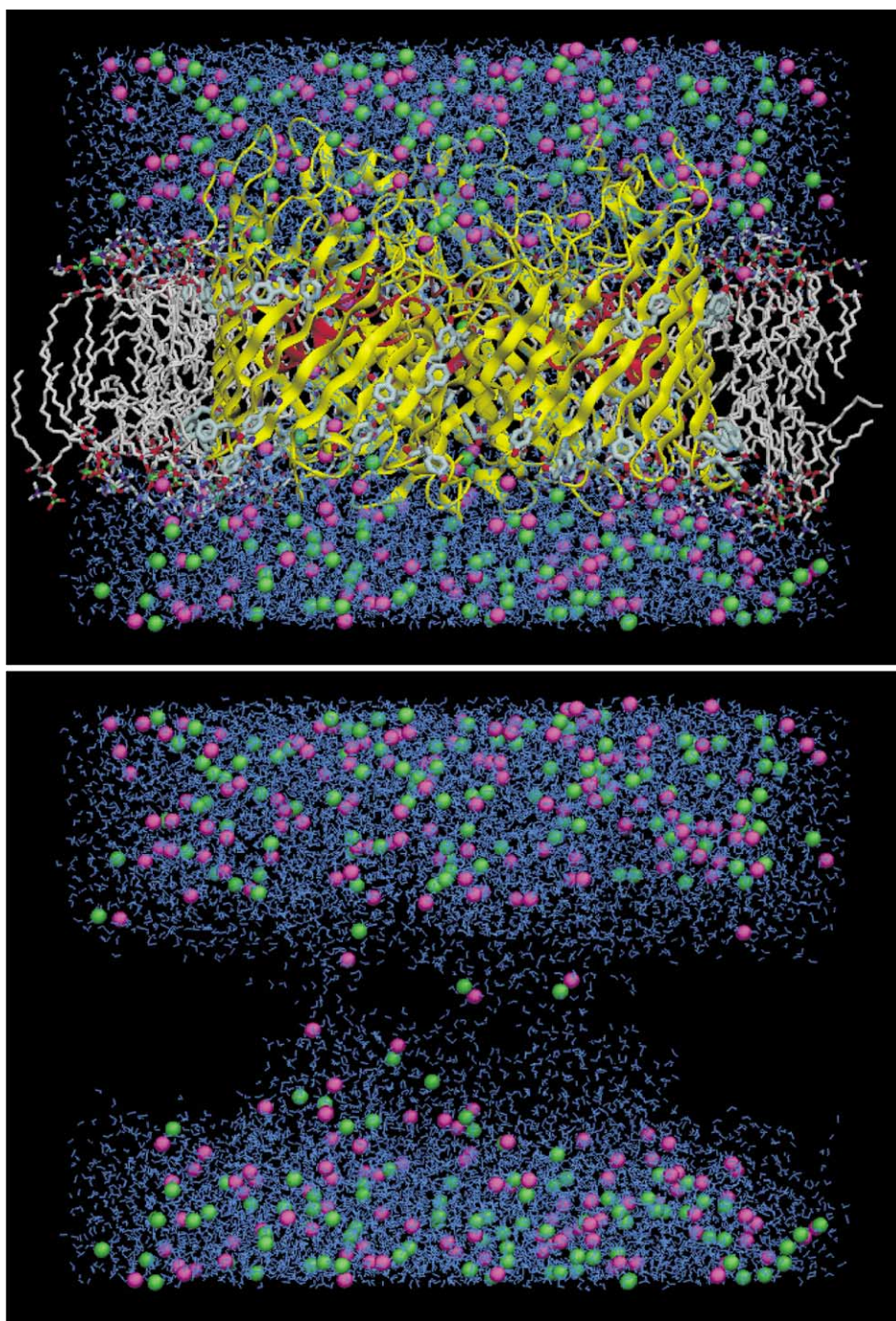
Figure 1. (top) Molecular graphics view of OmpF porin embedded in a DMPC membrane in an aqueous solution of 1M [KCl] salt (the K^+ are magenta and the Cl^- are green). For clarity, some lipid molecules were removed from the front view. The upper and lower aromatic girdles are well positioned within the hydrophobic core of the membrane. The infolding loop L3 is colored by red to show the constriction zone along the Z-axis. (bottom) The three large aqueous pores occupied by various ions are clearly shown without OmpF channel protein and the membrane. This snapshot was taken after the equilibration run. The Figure was produced with DINO (http://www.dino3d.org).

Simulation Methodology

Computational details

OmpF porin in a DMPC bilayer membrane with 1 M KCl salt

An instantaneous configuration of the atomic model of the fully hydrated OmpF porin-membrane system in 1 M KCl salt solution is shown in Figure 1(a). It comprises the OmpF trimer, 124 DMPC lipid molecules (64 and 60 in the upper and lower leaflets of the bilayer, respectively), 13,470 water molecules (including 330 crystallographic water), 231 K^+ and 201 Cl^-, for a total of 70,693 atoms. The corresponding configuration is shown without the porin and membrane in Figure 1(b). For the sake of convenience, the three OmpF monomers are referred to as M1, M2, and M3. Hexagonal periodic boundary conditions were applied to represent an infinite planar bilayer in the *XY*-direction with a center-to-center distance of 99.88 Å between the neighboring trimers and to simulate a periodic multilayer system along the *Z*-axis with an initial translation distance of 83.0 Å. The center of the membrane bilayer is located at $Z = 0$. The construction and equilibration of the complete OmpF system is described below (see Construction of the starting configuration).

After full equilibration a 5 ns MD trajectory of the OmpF system was generated. All calculations were performed using the CHARMM biomolecular simulation program.[36] The all-atom parameter set PARAM22 for protein[37] and phospholipids,[38] and a modified TIP3P water model[39] were used. The Lennard–Jones parameters for K^+ and Cl^- were adjusted to yield the experimental solvation-free energy in bulk water.[40,41] The trajectory was generated at constant normal pressure (1 atm), temperature (330 K), and cross-section surface area in the CPTA ensemble. The temperature was chosen to insure a fluid liquid-crystalline L_α phase for the DMPC membrane.[42] In this CPTA ensemble, the system's area is fixed but the height along the *Z*-axis changes to maintain the normal pressure.[43,44] The integration time step was 2 fs. All bond lengths involving hydrogen atoms were fixed using the SHAKE algorithm.[45] To remove the artifact associated with truncation of electrostatic forces, electrostatic interactions were calculated using the Particle–Mesh Ewald (PME) method with a $100 \times 100 \times 90$ grid for fast Fourier transforms (FFTs), $\kappa = 0.32$ Å^{-1} and a sixth-order B-spline interpolation.[46] The van der Waals energy was smoothly switched off at 8–10 Å by use of a switching function.[47] Any global translation of the OmpF trimer in the membrane plane was prevented by applying a cylindrical harmonic restraint to its center-of-mass in the *XY*-plane. The equilibration and the initial 2 ns production were calculated using 32 CPUs running in parallel on the IBM SP2 at the Cornell Theory Center (CTC).

Table 1. Summary of first and second peaks and minima of various RDFs in 1 M KCl aqueous solution

Pairs	r_{max}	$g(r_{max})$	r_{min}	$g(r_{min})$	$N(r_{min})$[a]
K^+–Cl^-	2.98	16.73	4.00	0.35	0.46
	5.32	1.95	6.45	0.95	1.17
K^+–O	2.72	4.57	3.57	0.44	6.46
	4.97	1.17	6.27	0.95	32.84
Cl^-–O	3.12	3.97	3.77	0.65	7.16
	5.52	1.06	6.22	0.95	31.68

[a] Integration number of an RDF up to its first (or second) minimum.

The following 3 ns production was calculated using 16 CPUs on the Origin 2000 at the National Center for Supercomputing Applications (NCSA). The atomic coordinates were saved every 50 step (100 fs) for analysis, producing 42.4 GB of data. A 50 ps production run took about 30 hours on the SP2 and 33 hours on the Origin 2000.

1 M KCl salt solution in bulk and in a DMPC membrane

Two additional simulations without OmpF were generated to validate the computational methodology and to supplement the information gained from the simulation of OmpF in a DMPC bilayer. First, a simulation of a 1 M KCl aqueous slat solution without any membrane was generated using the same simulation methodology and force field as described above. The system consists of 2556 water molecules, 50 K^+ and 50 Cl^- in a cubic box of 43.65 Å (initial size). After equilibration, a 2 ns trajectory was generated at constant pressure and temperature (CPT) according to the same conditions as in the OmpF simulation. A 100 ps production run took about 37 hours on a single Pentium III 700 MHz processor. The first and second peaks and minima of few selected radial distribution functions (RDFs) calculated from the simulation are summarized in Table 1. The first hydration shell extends up to 3.57 Å for K^+ and 3.77 Å for Cl^-. On average it contains 6.5 and 7.2 water molecules for K^+ and Cl^-, respectively. This is in good accord with experimental estimates, indicating that the hydration number is roughly to be 6–8 water molecules for K^+ and Cl^-.[48] The results were also compared with the average structure extracted from very recent neutron scattering experiments from a 1.25 M KCl salt solution by A. Soper (personal communication). The comparison revealed that both the position and the height of the main peaks in the RDFs of K^+–Cl^-, K^+–water oxygen, and Cl^-–water oxygen were in remarkably good agreement with the data (W.I. & B.R., unpublished results). This suggests that the most important structural features of the concentrated aqueous salt solution are reasonably well represented by the present atomic model. Furthermore, a simulation of a pure DMPC

Table 2. Protonation states of key titratable residues in OmpF porin

Residue	Current work	Karshikoff *et al.*[27]	Schirmer & Phale[15]
Asp37	-1	-0.7	-1
Asp74	-1	-0.5	-1
Asp126	-1	-1	-1
Asp127	-1	0	0
Asp312	0	0	0
Glu296	0	0	0
Arg82	$+1$	0	$+1$
Arg167	$+1$	0.2	0
Arg168	$+1$	$+1$	$+1$

membrane bathed by the same 1 M KCl solution, but without any porin, was also generated. The system comprises 72 DMPC molecules (36 in the upper and lower leaflets of the bilayer, respectively), 2872 water molecules, 50 K^+ and 50 Cl^- in an orthorhombic box of 48 Å × 48 Å × 76 Å (initial size). After equilibration, a 2.5 ns trajectory was generated in the CPTA ensemble according to the same condition as in the OmpF simulation. A 100 ps production run took about 80 hours on a single Pentium III 700 MHz processor.

Construction of the starting configuration

OmpF porin trimer

The initial configuration of the OmpF trimer was taken from the X-ray structure (PDB entry 2omf). The standard protonation state corresponding to pH 7 was used except for Glu296 and Asp312, which were protonated, so that the net charge of the OmpF trimer is $-30e$. For the sake of comparison, Table 2 shows the protonation states of some residues which were used in the previous work of Schirmer and co-workers.[15,27] The trimer was centered at the origin and its threefold symmetric axis was directed along the Z-axis with the extracellular side at $Z > 0$. The position of the trimer along the Z-axis was determined using the distribution of the hydroxyl oxygen atoms of tyrosine side-chains forming upper and lower girdles of aromatic residues at the solvent–membrane interface. The orientation of the side-chain of Tyr157, initially facing the hydrophobic core of the membrane in the crystallographic structure, was modified on the basis of another crystal structure of OmpF with a different crystal space group (PDB entry 1opf) such that its hydroxyl oxygen atom points toward the solvent-membrane interface. The position of OmpF embedded in the membrane ranges roughly from -24 Å to 36 Å along the Z-axis.

DMPC bilayer

Because the protocol for constructing a starting configuration of a membrane protein simulation has been discussed in detail previously,[49–52] only the main steps are described briefly.† First, The number of lipids and the system size in the XY-plane were determined using the cross-section area of OmpF along the Z-axis. The cross-section area corresponding to the upper and lower aromatic girdles is 4563 Å² and 4847 Å², respectively. Since the cross-section area of one DMPC in the liquid-crystalline L_α phase is approximately 64 Å²,[42] the difference between the upper and lower areas corresponds to the cross-section of about four DMPC molecules. To surround OmpF by at least two layers of lipid in the plane of the membrane, the primary system was constructed with 64 and 60 DMPC molecules in the upper and lower leaflets of the bilayer, respectively. The total cross-section area of the system is roughly 8639.5 Å², corresponding to a center-to-center distance of 99.88 Å between the neighboring trimers in the XY-plane under hexagonal periodic boundary conditions. The initial XY positions for each lipid were determined using 124 large Lennard–Jones spheres restrained harmonically on two layers ($Z = \pm 12$ Å) in the presence of hexagonal periodic boundary conditions. The spheres were then replaced by pre-equilibrated and pre-hydrated DMPC molecules randomly taken from a set of 2000 DMPC molecules.[53] The initial configuration was then refined by reducing number of unrealistic hard core overlaps between heavy atoms using systematic rigid body rotations and translations, and a series of energy minimizations. Finally, after overlays of K^+, Cl^-, and water molecules (see below), the starting configuration of the system was relaxed and equilibrated with various restraints for 250 ps at constant volume using Langevin dynamics with an integration time step of 1 fs according to a protocol developed previously.[54] Positional harmonic restraints for side chain and heavy atoms of OmpF were applied and reduced progressively to prevent sudden distortions relative to the X-ray structure. To maintain the overall structure of the lipid bilayer, planar harmonic restraints were applied to center-of-mass coordinates of DMPC headgroups away from $Z = \pm 17$ Å and reduced gradually over the 250 ps dynamics. The penetration of bulk water into the hydrophobic core of the DMPC bilayer was prevented using a half-harmonic repulsive planar potential. Additional water molecules were added to establish the density of bulk water after both 150 ps and 200 ps equilibration. The system, simulated for 250 ps at constant volume, was followed by an additional 100 ps equilibration at constant pressure and temperature (CPTA ensemble). As seen in Figure 1(a), the porin fits very well in the DMPC bilayer. In particular, the position of the upper and lower girdles of aromatic residues at ± 12 Å along the Z-axis near the solvent–membrane interface matches perfectly the

---

† A copy of all the CHARMM scripts needed can be found at http://thallium.med.cornell.edu/RouxLab
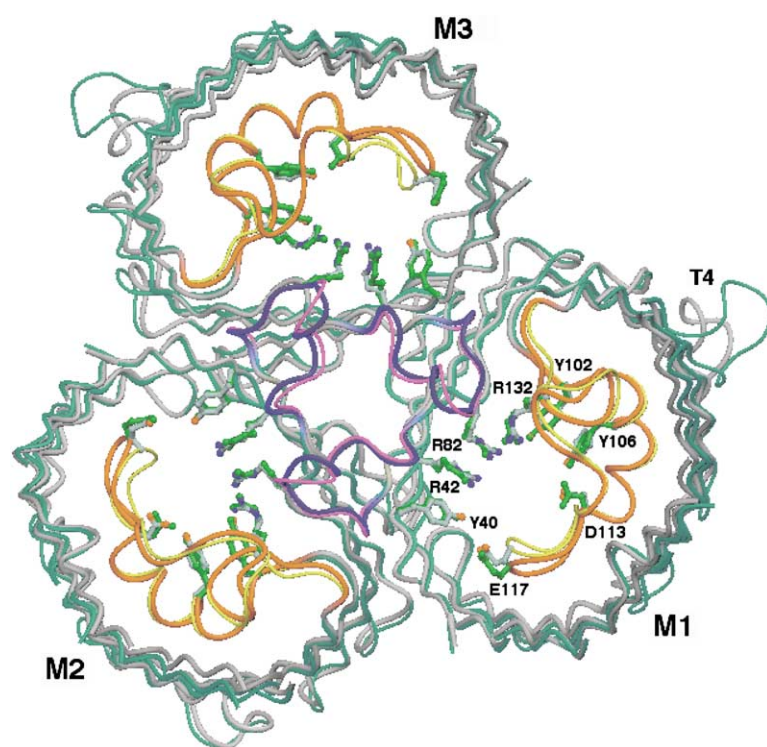
Figure 2. A superimposition of the OmpF C$^\alpha$ atoms. The X-ray structure is colored by gray and the average structure of the 5 ns trajectory by cyan: loop L2 is colored by blue for the X-ray structure and by magenta for the average structure, and loop L3 is colored by red for the X-ray structure and by yellow for the average structure. Each monomer is labeled as M1, M2, and M3. The key residues in the constriction zone are shown as labeled ball-and-stick models (green for the X-ray structure). For clarity, all the loops except L2 and L3 are not shown. The Figure was produced with DINO (http://www.dino3d.org).

thickness of the hydrocarbon core of a DMPC lipid bilayer.[24,42]

Aqueous 1 M [KCl] salt solution in the OmpF system

By calculating the ion-accessible volume V_{ion} in the OmpF system, the number of ions corresponding to 1 M KCl salt ([C]) were determined as 231 K$^+$ and 201 Cl$^-$ from the following expressions:

$$N_K = [C]V_{ion} - Q_{OmpF}/2e$$
$$N_{Cl} = [C]V_{ion} + Q_{OmpF}/2e \tag{1}$$

where $Q_{OmpF} = -30e$ is the net charge of the porin (n.b., these expressions are obtained from constraints on the electroneutrality $N_K - N_{Cl} = -Q_{OmpF}/e$, and the total number density $N_K + N_{Cl} = 2[C]V_{ion}$ deduced from linearized PB theory). It can be shown that the number of ions given by these expressions is consistent with an integration of the spatial ion density calculated from a linearized PB equation. The ion-accessible volume, $V_{ion} = 358943.5 \text{ Å}^3$, was calculated using a $187 \times 187 \times 167$ orthorhombic grid with a grid spacing of 0.5 Å (the dimension of this orthorhombic cell was chosen to have the same volume as that of the hexagonal system). For this calculation, the OmpF porin as well as the DMPC lipids were represented explicitly. To obtain a reasonable starting configuration of the 231 K$^+$ and 201 Cl$^-$, a Metropolis Monte Carlo simulation of the ions was performed with a fixed membrane and porin using the electrostatic potential calculated numerically from the Poisson equation.[31,32]

The electrostatic potential was calculated on the same grid as in the accessible volume calculation using the PBEQ module[55–57] in CHARMM.[36] The aqueous pore of each monomer was then filled by water molecules through overlays of an equilibrated cylinder with water of 16 Å radius and 60 Å height. The crystallographic water molecules were kept except those located at a position corresponding to the hydrocarbon core region of the membrane (18 molecules out of 128 per monomer). Finally, the entire system was hydrated with a pre-equilibrated hexagonal water box. The simulation system including the solvent regions ranges roughly from -36 to $+47$ Å along the Z-axis.

Results and Discussion

Dynamics of OmpF porin

An instantaneous configuration of the simulated OmpF system is shown in Figure 1(a) and (b). The membrane and the protein were observed to be very stable during the simulation with no extensive penetration of ions or water molecules into the hydrophobic core of the membrane. In particular, the OmpF porin remained very close to the X-ray structure with a relative root-mean-square (RMS) backbone deviation of only 1.4 Å. The average MD and X-ray structures are compared in Figure 2 and the RMS deviations of the main structural elements of OmpF are given in Table 3. As expected, the transmembrane β-barrel is the most stable, exhibiting deviations significantly smaller than those of the long extracellular loops (L1–L8) as well as the short periplasmic turns (T1–T8).

Table 3. RMS deviations relative to the X-ray structure (in Å)

Monomers	All atoms	Backbone	β-Barrel	Loops	Turns
M1	1.68	1.43	0.84	1.65	2.62
M2	1.67	1.32	0.77	1.87	1.02
M3	1.63	1.41	0.87	1.65	2.48

Averages were calculated using all the non-hydrogen atoms.

The turn T4 monomers M1 and M3 as well as the loops L1 and L5–L8 deviated slightly more from the X-ray structures, possibly because of differences in the crystallographic and membrane environment. For example, loops L6–L8 are involved in protein–protein contact with the turns T6–T8 in the crystal, while they are free in bulk solution in the simulated system. One may also note that the simulation was carried out at a temperature (330 K) that is higher than the liquid nitrogen temperature (77 K) at which the crystallographic structure was determined.[5]

The calculated RMS fluctuations of the proteins are shown in Figure 3. All three monomers show very similar fluctuations during the simulation, indicating that the trajectory provides an adequate conformational sampling of the protein (differences in the average properties of the three identical monomers can be used to assess the statistical convergence of the trajectory). The accord between the RMS fluctuations calculated from the MD and those estimated from the crystallographic Debye–Waller B-factors is generally good, though the extracellular loops and periplasmic turns are more flexible in the simulation. The discrepancies may be explained by differences between the crystal
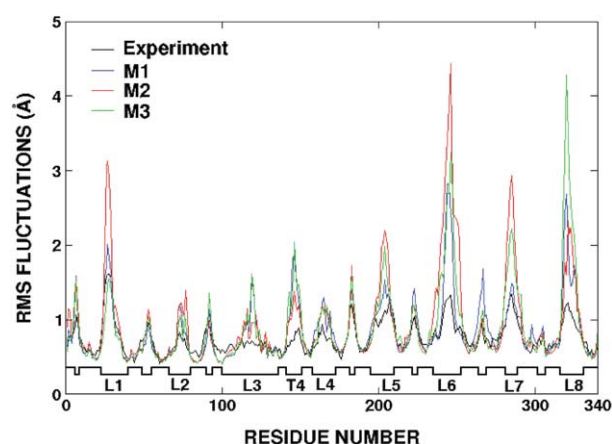
Figure 3. RMS fluctuations of the backbone atoms calculated from the MD sumulation (monomers M1, M2, and M3) and from the experimental B-factors. The RMS fluctuations of the ith protein atom were estimated from the crystallographic Debye-Waller B-factors,[28] $\langle \Delta r_i^2 \rangle = (3/8\pi^2)(B_i - B_{stat})$ where B_{stat} represents the effect of static disorder in the crystal. A uniform offset constant of 0.28 Å was subtracted from the X-ray data to take the presence of static disorder into account. The values were averaged over each residue.

and fluid membrane environment (see above). Similar trends were observed in the MD simulation of Tieleman & Berendsen.[30]

The residues contributing significantly to the stability of the trimer remained very close to the X-ray structure and have significantly smaller fluctuations than the rest of the structure. A number of residues form a nonpolar core near the trimeric symmetry axis (e.g. Ile3, Leu13, Leu43, Trp61, Tyr63, and Phe65). In this case, the deviations relative to the X-ray structure are only on the order of 0.5 Å RMS with fluctuations of the order of 0.8 Å. In addition, the loop L2 of monomer M1 reaches over to form strong polar interactions with several residues of monomer M2 (see Figure 2). Most of them remained very stable and close to the X-ray structure during the simulation. For example, strong salt bridges between Glu71 in loop L2 and Arg100 and Arg132 of the neighboring monomer are extremely stable throughout the simulation, consistent with the experimental observation that the denaturation temperature of an E71Q mutant is decreased from 72 to 48 °C.[58]

The deviations of the average dynamical structure relative to the crystallographic structure near the constriction zone are dominated by the fluctuations of the short polypeptide segment located at the tip of L3. As shown in Figure 2 this segment, which comprises the residues Pro116-Glu117-Phe118-Gly119-Gly120 (PEFGG), lines the narrowest part of the pore. The short segment interacts with the wall of the β-barrel through side chain (Glu117 to those Tyr22 and Tyr310) and backbone (Glu117 and Phe118 to Asp312) hydrogen bonding, and aromatic side-chains stacking (Phe118 with Tyr 22 and Tyr32).[5,27] All those interactions are seen to undergo dynamical fluctuations during the trajectory. Furthermore, a few water molecules make short transient excursions between the PEFGG segment and the wall of the β-barrel, hydrogen bonding with the side chain of Glu296 and Asp312, thereby further increasing the structural flexibility of this region. In contrast to the dynamical trajectory, no water molecules were detected at those positions in the crystallographic structure. The largest deviations of PEFGG (on the order of 4 Å) are observed for Pro116 which is maintained in place through relatively weak nonpolar interactions with Ala299, Thr300 and Tyr310 of the wall of the β-barrel. For all the other residues of PEFGG, the deviations relative to the crystallographic structure are less than 2 Å. In earlier studies, the movements of loop L3 were thought to be responsible for the observed voltage-gating of porins.[20–22] However, as observed from Figure 2, no large movements of L3 occurred during the current simulations, consistent with the experimental results of Phale *et al.*[19] and Bainbridge *et al.*,[23] and the MD simulation of Tieleman & Berendsen.[30]
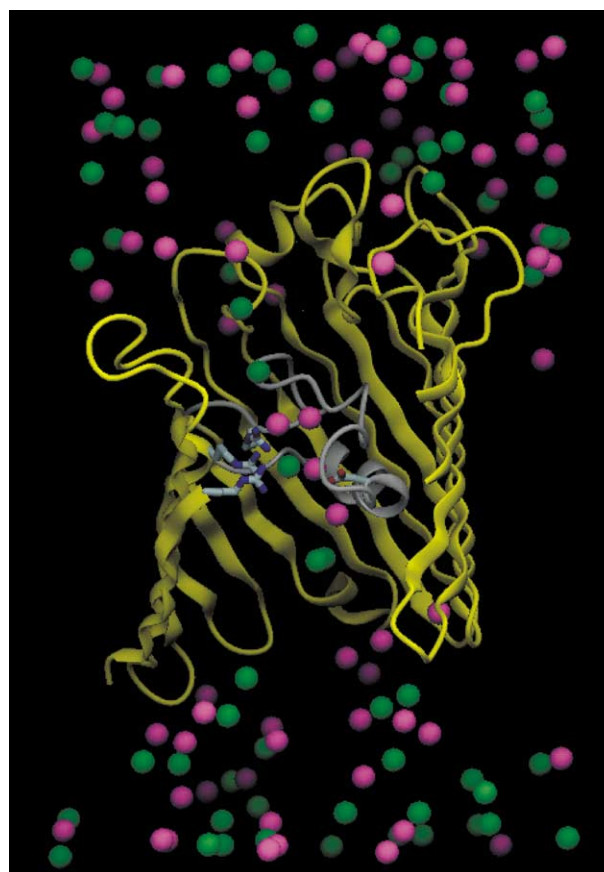
In contrast to loop L3, the cluster of three charged arginine (Arg42, Arg82, and Arg132) in the constriction zone is very stable during the
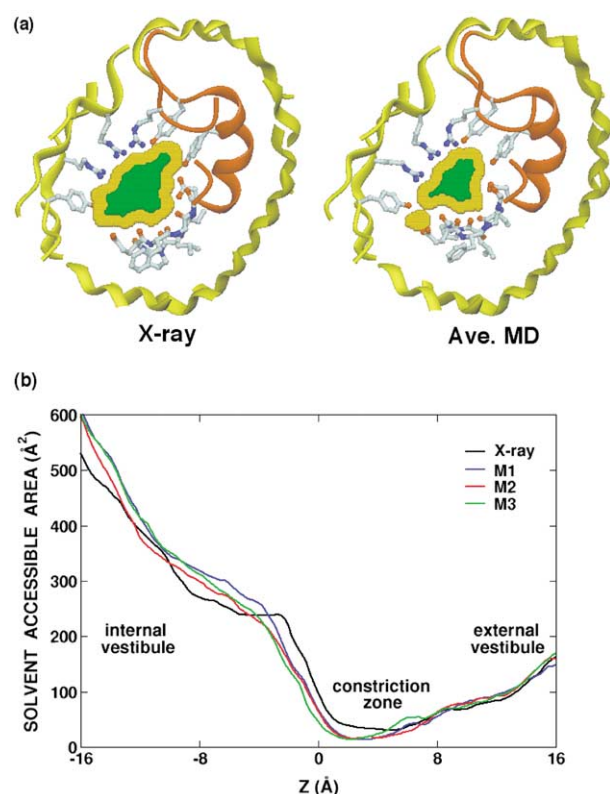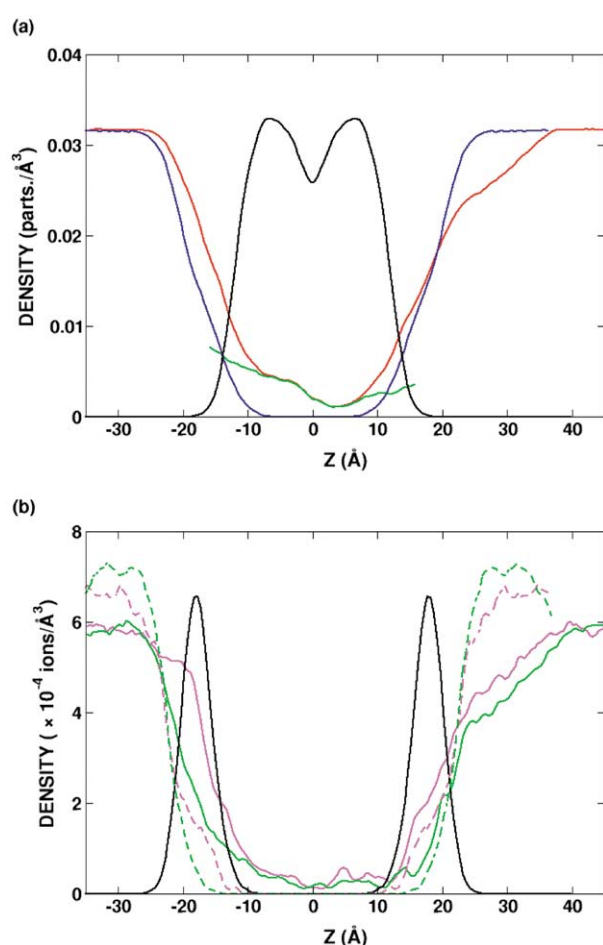
Figure 4. Cross-section area of the OmpF pore. (a) Two different ways of calculating the cross-section area are considered for the X-ray and average MD structures. The surface in green represents the cross-section area defined by the "solvent-accessible" region. The CHARMM PARAM22 Lennard-Jones radii scaled by $2^{-1/6}$ and augmented by a probe radius of 1.4 Å were used to define the "solvent-accessible" surface. The surface in orange represents the cross-section area defined by the protein "molecular" surface (van der Waals contact surface plus reentrant surface as probed by a sphere of 1.4 Å radius).[77,78] (b) Solvent accessible cross-section areas (along the Z-axis) of the 5 ns averaged structure of each monomer (M1, M2, and M3) and the X-ray structure. The OmpF channel pore is defined as the part of the channel bounded by the edges of the β-barrel spanning from −16 to +16 Å along the Z-axis. Three main regions can be distinguished: the wide intracellular vestibule (−16 Å < Z < 2 Å), the narrow constriction zone (2 Å < Z < 6 Å), and the extracellular vestibule (6 Å < Z < 16 Å). The area of the pore was calculated with a grid-based search (with spacing of 0.25 Å).

Figure 5. A snapshot of ions around monomer M1 at $t = 3.85$ ns (the K^+ are magenta and the Cl^- are green). For clarity, some residues in monomer M1 were removed from the front view. The infolding loop L3 is colored by gray. The key residues such as Arg42, Arg82, Arg132, and Asp113 are shown as stick models. The Figure was produced with DINO (http://www.dino3d.org).

simulation; the RMS fluctuations are in the order of 0.7 Å and the deviations are 0.6 Å for the side chains. Previously, Karshikoff *et al.* argued on the basis of continuum electrostatic calculations that Arg82 had to be uncharged (see Table 2).[27] More recently, Schirmer & Phale have revised the prediction from the calculations and concluded that the cluster must be fully charged based on the titration experiment of the ion selectivity of OmpF.[15] The stability of the cluster in the current simulation strongly suggests that three fully charged arginines are completely consistent with the crystallographic structure.

In Figure 4, the cross-section area near the constriction zone of the OmpF pore of the X-ray and average MD structures are compared. On average the constriction zone appears to be narrower in the dynamical trajectory than the fixed X-ray structure by about 15–25 Å²: the cross-section area corresponding to the solvent accessible and the molecular surface are 31 Å² and 80 Å² for the X-ray structure, and 15 Å² and 55 Å² for the average dynamical structure, respectively. During the simulation, the width of the pore fluctuates to values up to that of the X-ray structure during a few instantaneous configurations. The variations in the width of the constriction zone are directly related to the localized fluctuations of Pro116 in the short PEFGG segment (see above). A similar trend was observed in the MD simulation of Tieleman & Berendsen,[30] with the fluctuations of the residues of the PEFGG segment causing a narrowing of the constriction zone. Such a narrowing of the constriction zone, though significant, corresponds roughly to the size of a single water molecule and is not sufficient to prevent the

Figure 6. Calculated density profiles of ions and water molecules. All the density profiles were normalized using the cross-section area of the corresponding simulation systems. (a) Density profiles of water in the OmpF system (red) and the pure DMPC membrane system (blue). Green represents only the pore water. For comparison, the density profile of the hydrocarbon chain (black) in the pure membrane system is also shown. (b) Density profiles of K^+ (magenta) and Cl^- (green) in the OmpF system (continuous lines) and the pure DMPC membrane system (broken lines). For comparison, the density profile of the phosphate group (black) in the pure membrane system, which is scaled by 20, is also shown.

passage of ions and water molecules through the pore (see below). As seen from Figure 4(b), the aqueous pore of OmpF is markedly asymmetric, with a relatively small extracellular vestibule and a large and wide intracellular vestibule. A view of the ions in the pore of monomer M1 shows the wide extracellular and intracellular vestibules on both sides of the narrow constriction zone, as shown in Figure 5.

Water and ions inside OmpF pore

The configuration of the simulated system without the porin and membrane lipids shown in Figure 1(b) reveals the three wide asymmetric
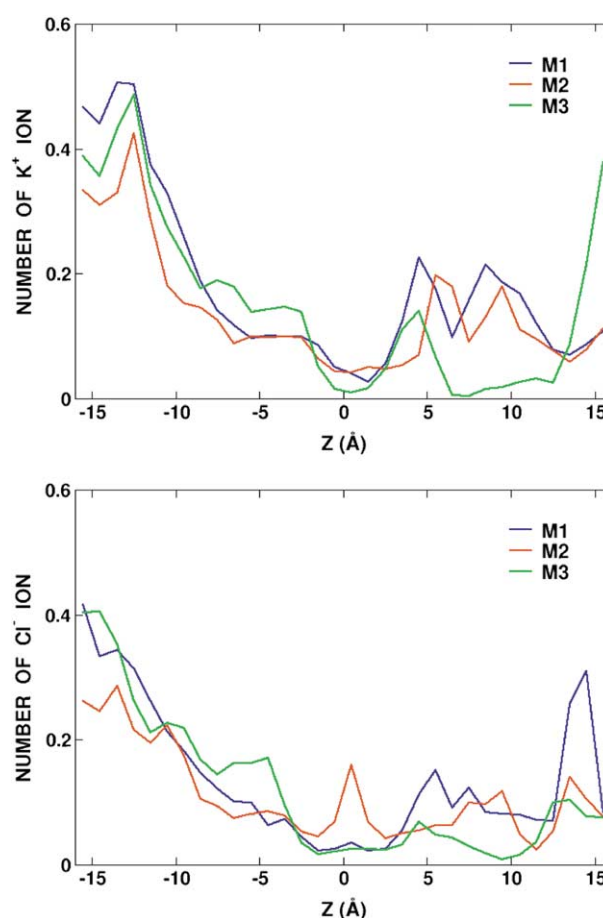
Figure 7. Average number of ions in each monomer (M1, M2, and M3) along the Z-axis. The number was calculated using a 1.0 Å bin along the Z-axis.

aqueous pores occupied by K^+ and Cl^- and water molecules. We now examine in detail the average structural and dynamical properties of the ions and water molecules inside the pores.

Water and ion density profile

The density profile of the water molecules and the ions in the OmpF pore are shown in Figure 6(a) and (b), respectively. Overall, the density profiles along the Z-axis is consistent with the asymmetric cross-section area of the pore (see Figure 4). On average, there are 236 water molecules in the intracellular vestibule, 14 water molecules in the constriction zone, and 74 water molecules in the extracellular vestibule, for a total of 324 water molecules inside the pore region of a single monomer (the regions are defined according to Figure 4). Similarly, a larger number of ions are found on the periplasmic side than on the extracellular side, because of the asymmetric shape of the pore. The distributions of ions in each of the three pores is shown in Figure 7. The average number of K^+ and C^- in each pore are 5.8 and 4.4 (M1), 4.5 and 3.6 (M2), and 4.9 and

3.8 (M3) for the three monomers, respectively. The distributions of ions inside each pore are slightly different, indicating that the simulation length of 5 ns is still not sufficient to obtain well-converged averages. Nonetheless, the simulation does capture the preference of OmpF porin for cations. For comparison, the corresponding ion density profile in the case of the pure DMPC membrane system bathed by the same salt solution is also shown in Figure 6(b) (the ion density is slightly higher than 1 M in the bulk solutions surrounding the membrane due to a redistribution of the ions during the simulation). It is clearly observed that the presence of OmpF increases significantly the accessibility of ions to the membrane region. Because of the character of the phosphatidylcholine polar headgroup of DMPC, K^+ are attracted by the negatively charged phosphate group which is located deeper than the positively charged choline group. They spontaneously partition deeper at the membrane–solvent interface than Cl^-; in a pure membrane system, there are 3.8 K^+ and 1.2 Cl^- in the slab $-20\,\text{Å} < Z < 20\,\text{Å}$. The water density is slightly reduced relative to the bulk on the extracellular side ($Z > 20\,\text{Å}$) due to volume occupied by the long loops in Figure 6(a), where the density profile of water in a pure DMPC membrane is also shown. In a pure lipid membrane system, water molecules can form hydrogen bonds with the lipid carbonyl group and penetrate up to the edge of the hydrophobic core region.[59] Because of the wide aqueous pore, a higher density is found at the membrane–solvent interface in the OmpF system than in the DMPC membrane system.

Orientation of water molecules in the pore

The probability distribution of the orientation of water dipoles along the Z-axis of the OmpF system is show in Figure 8. For comparison the distribution in the case of a pure lipid membrane is also shown in Figure 8(a). It is observed that there is little or no preferential orientation of water dipoles in the bulk regions. In the pure membrane system, the water molecules near the membrane–solution interface (i.e. $Z = \pm20\,\text{Å}$) have a high propensity to form a strong hydrogen bond with the lipid phosphate group, leading to dipole moments that are preferentially oriented perpendicular to the membrane surface. Further into the headgroup region (around $\pm12\,\text{Å}$), the water molecules are also preferentially oriented perpendicular to the Z-axis, but the water oxygen molecules points toward the membrane interior because of the lipid carbonyl groups. Similar results have been observed with DMPC bilayer with no salt.[59,60] Comparatively, the water dipoles are perturbed much more strongly by the membrane headgroup than by OmpF porin near the membrane–solution interface. This orientational effect of the lipid headgroup is reduced in the OmpF/DMPC system because the water molecules near or inside the aqueous OmpF pore are more or less free to
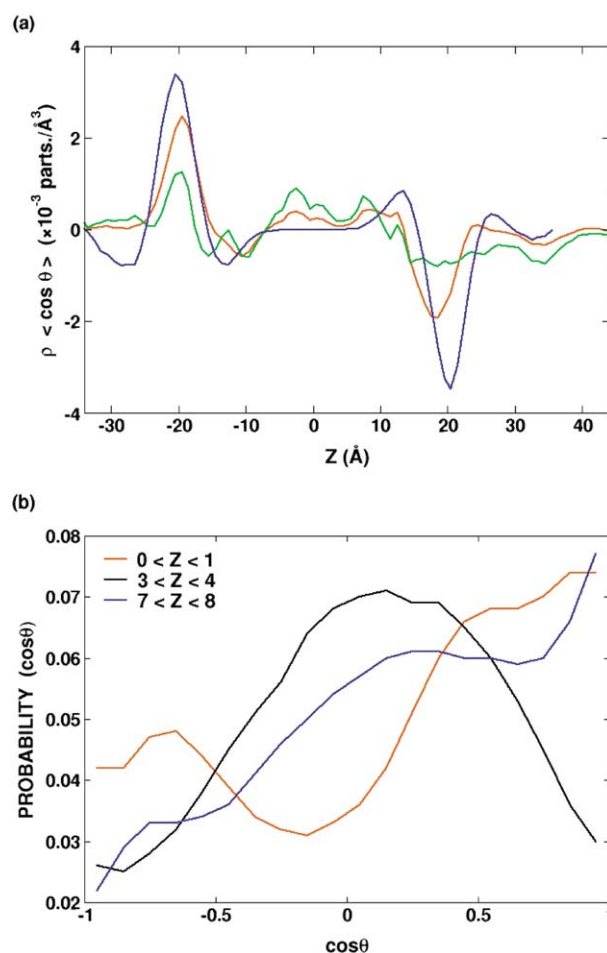
Figure 8. (a) Density-weighted water polarization profiles in the OmpF system (red) and the pure DMPC membrane system (blue). Green represents the polarization only from a cylindrical region of 35 Å radius encompassing roughly the whole OmpF trimer. $\langle\cos\theta\rangle$ is the average Z component of the water dipole, i.e. $\cos\theta = 1.0$ if the water dipole is parallel with the Z-axis, $\cos\theta = 0.0$ if the water dipole is perpendicular to the Z-axis, and $\cos\theta = -1.0$ if the water dipole is anti-parallel with the Z-axis. (b) Probability distribution of the Z component of the water dipole near the constriction zone ($3\,\text{Å} < Z < 4\,\text{Å}$). The definition for $\cos\theta$ is the same as in (a).

reorient. In contrast, the distribution of the water molecules is markedly anisotropic in the narrowest region of the aqueous pore. As shown in Figure 8(b), the most probable orientation of the water molecule in the constriction zone is perpendicular to the channel axis. The anisotropic distribution is caused by the strong transversal electrostatic field arising from the arginine cluster (Arg42, Arg82, and Arg132) and the two acidic residues (Asp113 and Glu117) on L3. This is illustrated in Figure 9 by showing an instantaneous configuration of the water molecules near the constriction zone of monomer M1. Just above and below the constriction zone, the dipoles of the water molecules are preferentially oriented towards the extracellular
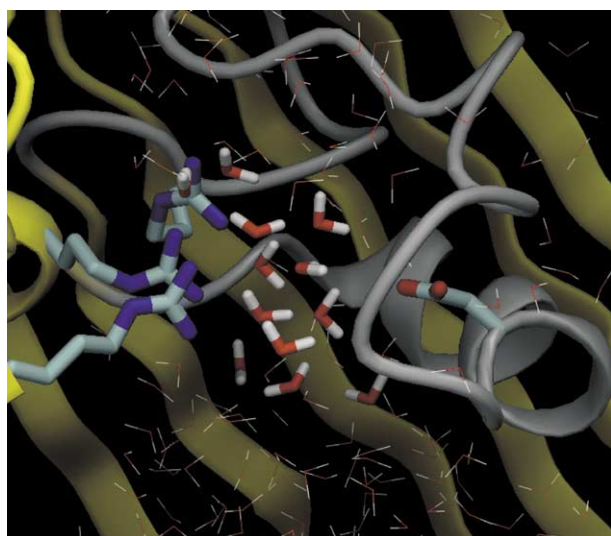
Figure 9. A snapshot of water molecules around the constriction zone of monomer M1 at $t = 1.2$ ns. For clarity, some residues in monomer M1 were removed from the front view. The infolding loop L3 is colored by gray. Some water molecules between 0 Å and 8 Å along the Z-axis are highlighted by stick models to clarify the preferential orientation of water dipoles around the constriction zone (see Figure 8(b)). The key residues such as Arg42, Arg82, Arg132, and Asp113 are shown as stick models. The figure was produced with DINO (http://www.dino3d.org).

side, i.e. the water oxygen molecules most probably point toward periplasmic side. The water molecules adopted a similar orientation in the constriction zone in the MD simulation of Tieleman & Berendsen,[30] although the opposite orientation was seen below and above (i.e. water dipoles preferentially orients towards the intracellular side). The discrepancy may have been caused by differences in the protonation state of ionizable residues (e.g. the arginine cluster was not fully charged), the use of a cut-off in the electrostatic interactions (10 Å and 18 Å for short-range and long-range Coulomb interactions, respectively), and the small number of explicit cations in the simulation (only 27 Na$^+$).

Average ion pathways

Figure 10 shows the time-dependent displacement of specific K$^+$ and Cl$^-$ along each of the three pores during the 5 ns dynamics. A few particularly notable events are observed (not shown for the sake of clarity are a large number of ions which visit the extracellular and intracellular vestibules). One K$^+$ and two Cl$^-$ translocated from the extracellular side to the periplasmic side through the pore of monomer M1, the K$^+$ (red) remaining in the constriction zone over 3 ns. Only one K$^+$ (blue) exhibits an incomplete translocation through the pore of monomer M2, going from the external vestibule to the internal vestibule and returning to the constriction zone. One K$^+$ and one Cl$^-$ trans-
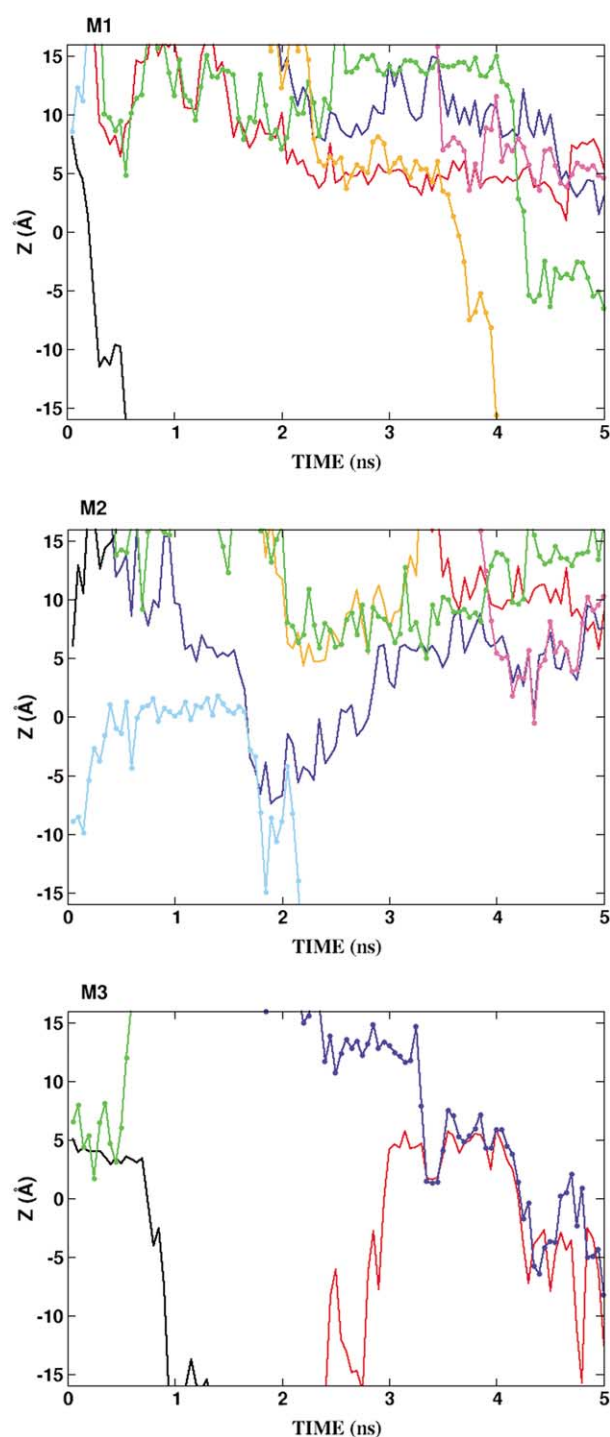
Figure 10. Displacement of K$^+$ and Cl$^-$ through each monomer (M1, M2, and M3) along the Z-axis. Different colors represent different ions: no symbol for K$^+$ and sphere for Cl$^-$. For clarity, only a few selected ions are shown in each plot.

located from the extracellular side to the periplasmic side through the pore of monomer M3. It is possible to characterize the OmpF pores in terms of average properties from the present calculations despite the relatively small number of completed translocation events. For example, the
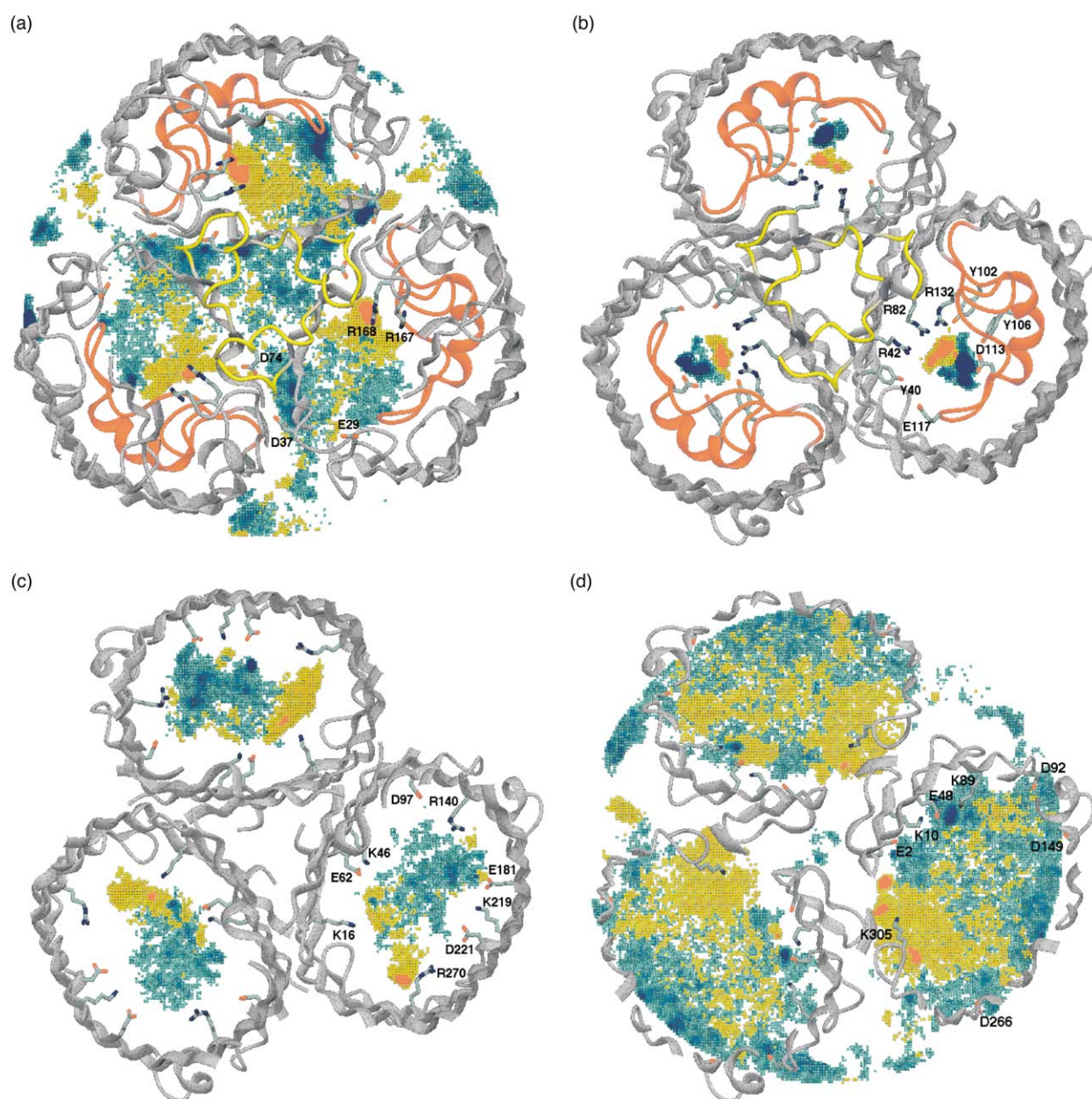
Figure 11. Ion density maps on the *XY* plane at the different positions along the *Z*-axis, calculated using a $211 \times 211 \times 11$ grid (with grid spacing of 0.4 Å) corresponding to a slab of 4 Å thickness; (a) in the extracellular vestibule (between $Z = 22$ and $Z = 18$ Å), (b) in the constriction zone (between $Z = 6$ and $Z = 2$ Å), (c) in the pore periplasmic side (between $Z = -2$ and $Z = -6$ Å), and (d) in the periplasmic vestibule (between $Z = -14$ and $Z = -18$ Å). The key residues are shown as labeled ball-and-stick models. The K^+ density ρ_{K^+} (parts./Å^3) is represented by cyan ($\rho_{K^+} = 0.0006$) to blue ($\rho_{K^+} = 0.006$) and the Cl$^-$ density ρ_{Cl^-} (parts./Å^3) by yellow ($\rho_{Cl^-} = 0.0006$) to red ($\rho_{Cl^-} = 0.006$). The Figures were produced with DINO (http://www.dino3d.org).

constriction zones of monomer M1 and M2 are occupied by several ions after 2–3 ns, even though no complete passage of an ion through any of the pores is observed thereafter.

To reveal the preferred pathway for ion translocation and help identifying key residues playing an important role in ion permeation, the average ion density in the cross-section of the pore was calculated at the different position along the *Z*-axis. The results are shown as two-dimensional maps in Figure 11. Each map corresponds to the

ion density within a specific range along the *Z*-axis: in the extracellular vestibule (a), in the constriction zone (b), in the pore on the periplasmic side (c), and in the periplasmic vestibule (d). In the constriction zone (Figure 11(b)), K$^+$ and Cl$^-$ are distinctly separated. The separation is caused by the strong transversal electrostatic field generated between the arginine cluster (Arg42, Arg82 and Arg132) and two acidic residues (Asp113 and Glu117) on L3 in the constriction zone.[5,15,27,31] On the periplasmic side of the constriction zone
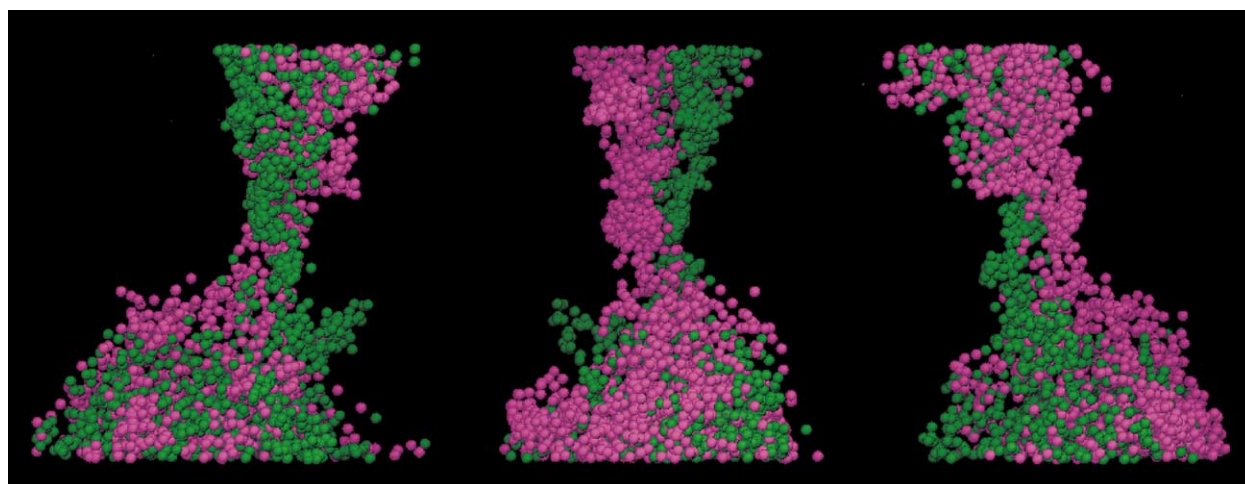
Figure 12. A superimposition of 100 snapshots of the ions in all three pores (the K^+ are magenta and the Cl^- are green) Each snapshot was extracted every 50 ps from the 5 ns trajectory and all the ions in monomers M2 and M3 were superimposed into monomer M1 by rotations. (left) View from the 3-fold symmetric axis. (middle) left view rotated by 120°. (right) left view rotated by 240°. The Figure was produced with DINO (http://www.dino3d.org).

(Figure 11(c)), there is an abrupt increase in the ion-accessible area and the maximum density of Cl^- is found between Lys16 and Arg270. Notably, the position of the density maximum is now rotated in a counter-clockwise direction relative to the position in the constriction zone. This rotation is apparently caused by stabilizing interaction with Glu62 which is located right below the arginine cluster. In the periplasmic vestibule (Figure 11(d)), Cl^- tend to stay near the barrel wall close to the basic residue (Lys10, Lys305, and others) near the 3-fold axis whereas K^+ tend to stay close to the acidic residues (Asp92, Asp149, Asp266, and others) near the outer rim of the pore. In the extracellular vestibule (Figure 11(a)), the highest density of K^+ is observed at the outer rim of the β-barrel (near Asp113, Glu117, and Asp121 on L3, and Glu29 on L1) and the monomeric interface (near Asp37 and Asp74). The region of high Cl^- density, well separated from that of K^+, is found above Arg167 and Arg168. No particular pattern is observed in the ion distribution in the bulk solution although K^+ has a slightly higher propensity than Cl^- to be located along the trimeric axis.

To visualize the average preferred pathway of K^+ and Cl^-, a superimposition of 100 instantaneous configurations of the ions in all three pores was constructed. The result is shown from three different points of view in Figure 12. It is observed that the K^+ and Cl^- pathways are very well separated and span over nearly 40 Å along the axis of the aqueous pore, roughly from $Z = -20$ Å to 22 Å. The charge separation exists throughout the pore, though it is more pronounced in the extracellular vestibule and the constriction zone than in the periplasmic vestibule (see also Figure 11). In the central region of the pore, K^+ and Cl^- follow two left-handed screw-like pathways, undergoing a counter-clockwise rotation of 180° from the extracellular vestibule to the pore

periplasmic side. Overall, there appears to be a good correspondence of high densities of K^+ and Cl^- with the positions of the charged residues in the OmpF structure, though it should be emphasized that the average pathways could not have been deduced easily from a simple inspection of the X-ray structure. The resulting average ion distribution arises not only from the strong transverse electric field in the pore, but also from the electrostatic interactions with a large number of residues. A similar transverse field was noted by Karshikoff et al.[27] on the basis of continuum electrostatic calculations. On the basis of this observation, they suggested that its role could be to facilitate the permeation of dipolar solutes. Nonetheless, the biological significance of this feature of OmpF is unclear. Perhaps the left-handed twist in the direction of the transverse field, shown here to extend nearly over 20 Å, adds to the stability of the right-handed β-barrel structure.

On the basis of this analysis, one can envision the average journey of K^+ and Cl^- from the extracellular side to the periplasmic side. K^+ preferably enter the external vestibule (mouth of pore) near the monomeric interface due to Asp37 and Asp74 or above the tip of loop L3 due to Glu29, and Asp121 and Glu117 on loop L3. In contrast, Cl^- preferably enter the mouth of pore following the electrostatic field generated by Arg167 and Arg168 (see Figure 11(a)). As they progress towards the intracellular side along the pore, the position of both ions is shifted in an anti-clockwise direction following the charged residues (see Figure 11(a) and (b)). The K^+ move down close to Asp113 on loop L3, while the Cl^- move down close to the arginine cluster along the barrel wall close to the 3-fold axis. After passing the constriction zone, the Cl^- continue down along the barrel wall toward Lys16 and Arg270 and away from Glu62, resulting again in an anti-clockwise rotation of more than

100° (see Figure 11(b) and (c)). The existence of two such well-separated pathways for cations and anions suggests that the charge specificity of OmpF porin does not arise from a few local interactions in the constriction zone, but rather from a large number of residue distributed over a large fraction of the aqueous pore. It would be interesting to examine mutations of charged residues along the average pathways (e.g. Lys16, Glu29, Asp37, Glu62, Asp74,[58] Arg167, and Arg168) and see how they effect the conductance and cation selectivity of the channel.
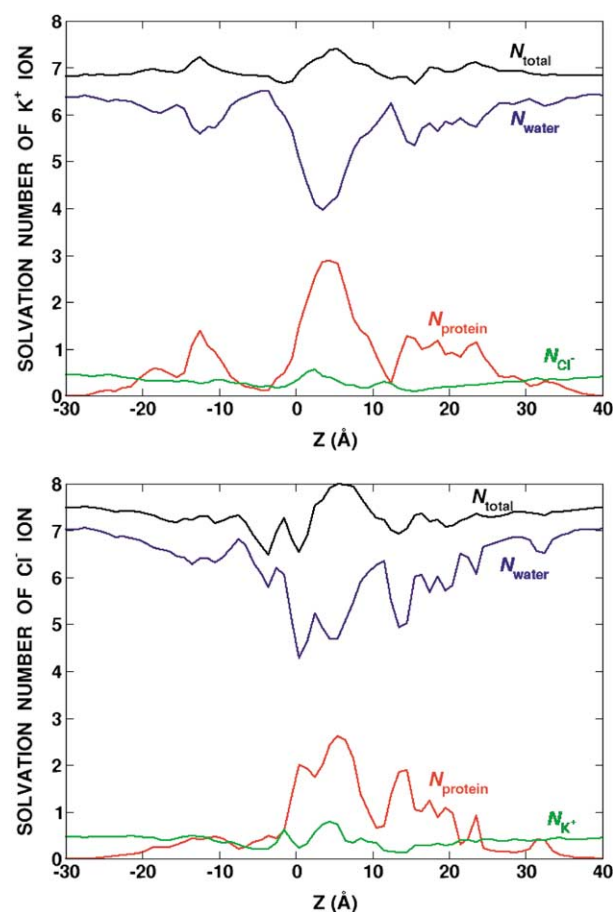
Ion solvation

One essential function of an ion channel is to progressively substitute favorable interactions for the loss of hydration.[61] To examine the variations in the solvation of the permeating ions, the number of water molecules, counter ions, and protein atoms around the ions were calculated as a function of their position along the channel axis. Only oxygen atoms were considered for the contribution from the protein to the solvation of K^+ and nitrogen atoms for that of Cl^-. The results are shown in Figure 13. It is observed that the hydration num-

ber of the ions is progressively altered in response to the change in the environment as they move into the OmpF pore. Interestingly, the contributions from water and the protein atoms appear to vary in a complementary fashion in order to keep the total solvation number of both ions approximately constant and similar to that in bulk solution throughout the channel. There are approximately four water molecules around both ions in the constriction zone where their hydration number appears to be minimum. This can be compared with the values in bulk solution, where there are roughly 6.5 and 7.2 water molecules in the first shell of K^+ and Cl^-, respectively (see Table 1). The contribution from OmpF to the solvation of both K^+ and Cl^- is somewhat asymmetric, i.e. more contributions in the external vestibule, because of the relatively narrow ion pathway in the external vestibule (see Figure 12). The net contribution from counter ions appears to be relatively small, although it is maximum in the constriction zone. This suggests that the pairing of K^+ and Cl^-, particularly in the narrowest part of the pore where their movements is the most restricted, could be important (see below).

Ion pairing

Traditional theories of ion permeation such as the Goldman–Hodgkin–Katz (GHK) equations are constructed on the assumption of ion independence.[61–63] This implies that the movements of ions are assumed to be uncoupled. Concerted movements of K^+ and Cl^- in the aqueous pore, such as those observed in Figure 10, represent a clear violation of ion independence. As illustrated in Figure 5, strong ion–ion coupling may occur when two ions are confined to move through the narrowest region of the pore. In this instantaneous configuration, a strongly interacting ion pair is shown in the constriction zone, with a K^+ located near Asp113 is less than 3.1 Å from a Cl^- located near the arginine cluster. More generally, one would expect strong ion–ion coupling even in a bulk aqueous salt solution due to the strong long-range electrostatic interactions. As shown in Table 1, in bulk solution those interactions are manifested in the ion–ion pair correlation between the different ions. According to the results of the simulation of a 1 M KCl solution, the fraction of ions in contact, which corresponds to the integral of the RDF $g_{K-Cl}(r)$ up to the first minimum, is equal to 0.46. This implies that almost half of the ions are involved in some form of counterion pairing in the 1 M KCl salt solution. Ion pairing can be further characterized by the number of the contact ion pair (CIP) (up to the first minimum of the RDF) and the number of the solvent separated ion pair (SSIP) (between first and second minima of the RDF).[64] A common quantity for analyzing the detailed pattern of ion pairing is the function $S_\alpha(n_1, n_2)$, corresponding to the frequency that the specific number of counter ions presents in CIP

Figure 13. Average first-shell solvation number of K^+ and Cl^- along the Z-axis. $N_{protein}$ was calculated using all kind of oxygen atoms for K^+ and all kind of nitrogen atoms for Cl^-.
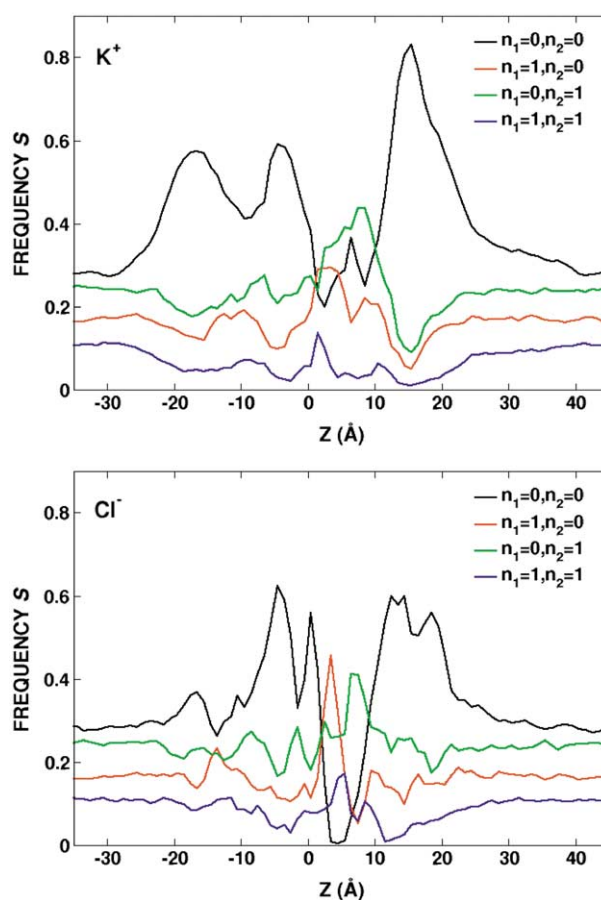
Table 4. The frequencies $S_{K^+}(n_1, n_2)$ and $S_{Cl^-}(n_1, n_2)$

	$n_2 = 0$	$n_2 = 1$	$n_2 = 2$	$n_2 = 3$	$n_2 = 4$
$S_{K^+}(n_1, n_2)$					
$n_1 = 0$	0.258	0.244	0.094	0.017	0.001
$n_1 = 1$	0.169	0.117	0.029	0.004	0.000
$n_1 = 2$	0.037	0.0.17	0.003	0.001	0.000
$n_1 = 3$	0.004	0.002	0.000	0.000	0.000
$S_{Cl^-}(n_1, n_2)$					
$n_1 = 0$	0.265	0.253	0.090	0.017	0.002
$n_1 = 1$	0.156	0.109	0.029	0.004	0.000
$n_1 = 2$	0.041	0.018	0.004	0.001	0.000
$n_1 = 3$	0.006	0.002	0.001	0.000	0.000
$n_1 = 4$	0.001	0.000	0.000	0.000	0.000

Figure 14. Profiles of few selected frequencies $S_{K^+}(n_1,n_2)$ (top) and $S_{Cl^-}(n_1,n_2)$ (bottom) along the Z-axis (for the definition of the frequency, see the text).

and in SSIP simultaneously, around a given ion of type α.[65] For example, $S_{K^+}(n_1 = 1, n_2 = 0)$ represents the frequency that a K^+ has one Cl^- in CIP and zero Cl^- in SSIP. As shown in Table 4, both frequencies for K^+ and Cl^- are very similar, showing roughly that 26% of ions do not have either CIP or SSIP, 16% of ions only one CIP, 25% of ions only one SSIP, 11% of ions both one CIP and one SSIP, and 22% of ions more than one CIP or SSIP. As a rare event, 0.3% of K^+ are embedded in three Cl^- in CIP and 0.6% of Cl^- ions in three K^+. Similar ionic clustering has been observed in other simulations of salt solution at high concentration.[65] The present observations about ion pairing in the 1 M KCl aqueous salt solution are strongly supported by the excellent agreement with recent neutron scattering data from A. Soper (personal communication).

Following a similar analysis, we calculated the frequencies of the first four types of ion pairing for K^+ and Cl^- along the OmpF channel axis. The results are shown in Figure 14. As shown in the variations of $S_{K^+}(n_1 = 0, n_2 = 0)$, and $S_{Cl^-}(n_1 = 0, n_2 = 0)$, ion pairing is significantly reduced in the membrane–solvent interface and inside the pore except in the constriction zone. The ion pairing corresponding to the 1 M KCl aqueous salt solution is recovered in the bulk region of the OmpF system (see Table 4). The dominant factor giving rise to a reduced ion pairing inside the pore is the fact that K^+ and Cl^- follow two distinct screw-like pathways on average. As seen in Figures 11 and 12, the passage of the ions through two separate pathways prevents the formation of ion pairs in the pore except in the narrow constriction zone where the two pathways come close together. One additional factor is the greater propensity of K^+ than Cl^- to partition at the membrane–solvent interface even without OmpF (see Figure 6(b)).

As indicated by $S_{K^+}(n_1 = 0, n_2 = 0)$, a K^+ can be found alone in the constriction zone about 30% of the time. In contrast, this is very unlikely in the case of Cl^-, as indicated by the very low value of $S_{Cl^-}(n_1 = 0, n_2 = 0)$, for the region corresponding to the constriction zone. One may also note that K^+ appear to be needed to accompany a Cl^- most of the time, as shown by the abrupt increase of CIP $(S_{Cl^-}(n_1 = 1, n_2 = 0))$ and SSIP $(S_{Cl^-}(n_1 = 0, n_2 = 1))$ in the constriction zone. Apparently, a Cl^- cannot go through the constriction zone alone without the presence of at least one K^+ (as a CIP or SSIP). This analysis suggests that the presence of K^+ in the OmpF pore is needed to screen the excess negative electrostatic potential arising from OmpF and helps the passage of Cl^-. These observations are consistent with the observation that OmpF is a cation-selective pore.[1,13,14]

Ion diffusion

The analysis of average structural quantities such as the density profiles shown in Figures 6 and 7, and the average pathways shown in Figures 11 and 12, provides important information on how OmpF functions as a molecular pore. However, these quantities which relate to the average structures and systematic average forces arising in the environment of the pore, are not sufficient to completely characterize the transport and permeation of ions.[66] The random chaotic movements of ions through a molecular pore is also affected by processes that are intrinsically dynamical and

dissipative.[67] In particular, the diffusion constant of the ions at different positions along the axis of the channel, $D(z)$, is a very important indicator of the ease with which the ions can move across the pore. Moreover, the diffusion constant of ions in the pore is a central input parameter in many theoretical description of permeation.[31,32,68–72] For these reasons, its characterization from an all-atom simulation with explicit water molecules is very important.

At the microscopic level, the diffusion constant is generally defined in terms of the average mean-square displacement (MSD):[73]

$$D = \lim_{t \to \infty} \frac{\langle [z(t) - z(0)]^2 \rangle}{2t} \qquad (2)$$

where the time t has to be large compared to the relaxation times of microscopic processes in the solution. Though it is rigorously valid only for a isotropic uniform environment, this expression is often used to calculate the space-dependent diffusing constant $D(z)$ of ions and water molecules in transmembrane pores.[30,70,72] Calculations based on equation (2) with a time $t \approx 10$ ps suggest that the diffusion constant of ions and water molecules is considerably reduced inside membrane channels to about 10% of its value in the bulk. This procedure, however, ignores the systematic influence of free energy barriers and wells on the local movements of ions at a specific position z along the permeation pathway.[67] For example, an ion may appear to diffuse slowly in a region of the pore, while in fact the small MSD is caused by the fact that it is trapped in a free energy well. For this reason, diffusion constants of ions in molecular pore extracted from equation (2) are probably underestimated. It is important to separate the local dissipative forces from the influence of the free energy profile for accurately extracting the diffusion constants which are then used in electro-diffusion theories or BD simulations. This problem can be addressed, at least in an approximate fashion, by considering an analogy with the random chaotic movements occurring during a BD trajectory of a particle along the axis z in a potential $W(z)$. Assuming that the particle is at position $z(t)$ at time t, according to the BD algorithm,[15,16,31,32] the next position of the particle at a time τ later is calculated as $z(t + \tau) = z(t) + \langle \Delta z \rangle + R$, where $\langle \Delta z \rangle = -DW'\tau/k_B T$ is the systematic displacement of the particle under the influence of the mean force $-W'$, and R is a Gaussian random number with zero mean and standard deviation $\langle R^2 \rangle = 2D\tau$. The diffusion constant is then estimated from the standard deviations of the displacement, $\Delta z(t) = z(t + \tau) - z(t)$:

$$D = \frac{\langle [\Delta z(t) - \langle \Delta z(t) \rangle]^2 \rangle}{2\tau} \qquad (3)$$

If the dynamical displacement reflected a purely Brownian motion, the choice of τ would be arbitrary. In reality, however, τ must be sufficiently large to incorporate all dynamical memory effects present in solution. According to the velocity auto-correlation functions of ions in solution, τ must be larger than about 0.5 ps.[64] On the other hand, τ should not be too large, since the analysis leading to equation (3) is based on the assumption of a small time-step τ. Interestingly, it can be shown that the result of equation (3) approaches that of equation (2) as τ is increased, in both cases the diffusion constant being calculated as an ensemble average over many ions. By trials and errors it is estimated that τ should be between 0.5 ps and 1.0 ps.

The profiles of the diffusion constant of K^+ and Cl^- along the channel axis were calculated using both equations (2) and (3). The results are shown in Figure 15. Both methods clearly indicate that the diffusion constant of the ions is reduced inside the OmpF channel. Although the overall patterns of the diffusion constant profiles are relatively similar to each other regardless of the method, the results differ significantly. The diffusion constants of K^+ and Cl^- are reduced to about 50% of their value in bulk solutions according to equation (3).
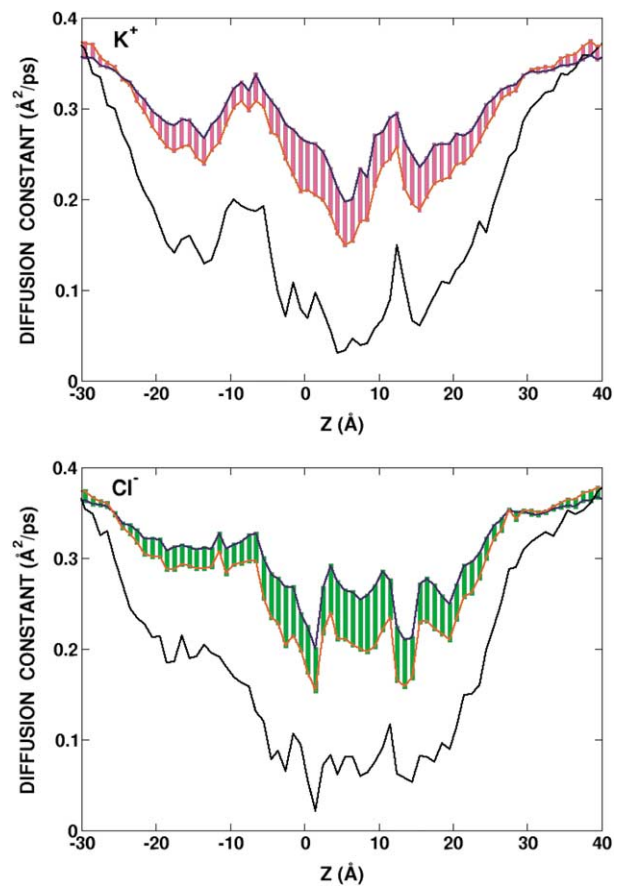
Figure 15. Profiles of the diffusion constant of K^+ (top) and Cl^- (bottom) along the channel axis. Black lines were calculated using equation (2) where the slope of $\langle [z(t) - z(0)]^2 \rangle$ versus t was calculated using the data for the interval 2–6 ps. Blue and red lines were calculated using equation (3) with $\tau = 0.5$ ps and $\tau = 1$ ps, respectively.

In contrast, equation (2) yields diffusion constants that are only 10% of their value in bulk solutions. Therefore, ignoring the systematic effect of the average forces as in equation (2) systematically underestimates the local mobility of the ions inside the pore. In the bulk region of the OmpF system, the results from equations (2) and (3) are virtually identical and the diffusion constants are roughly $0.37 \text{ Å}^2/\text{ps}$ for both ions. Similar values were calculated for the ions in the 1 M KCl bulk solution. The diffusion constants were also reduced by approximately 50% within 10 Å of the membrane–solution interface in the DMPC simulation without OmpF. It is likely that the slow diffusion is caused by the strong interactions of the water molecules and the ions with the lipid headgroups.

One may note that the calculated bulk diffusion constants are almost twice higher than the experimental values in 1 M KCl solution at 298 K, i.e. $0.185 \text{ Å}^2/\text{ps}$ (K$^+$) and $0.2 \text{ Å}^2/\text{ps}$ (Cl$^-$).[74] The relatively high temperature (330 K) in the current simulation and the fact that the diffusion constant of the water molecule based on the TIP3P potential is significantly over-estimated may both have contributed to the discrepancy.[60,75,76] For example, the diffusion constant of TIP3P water is $0.73 \text{ Å}^2/\text{ps}$, in the current simulation of 1 M KCl aqueous solution at 330 K, which is more than twice higher than the experimental value of $0.30 \text{ Å}^2/\text{ps}$ at 293 K. Nonetheless, although the absolute value of the estimated diffusion constants are quantitatively inaccurate, it is likely that the current results are qualitatively indicative of the variations of ion mobility throughout the OmpF pore.

Conclusion

A detailed atomic model of *E. coli* OmpF porin embedded in an explicit dimyristoyl-phosphatidyl-choline (DMPC) bilayer bathed by a 1 M [KCl] aqueous salt solution was constructed for MD simulations and a trajectory of 5 ns was generated and analyzed. The conformation of OmpF in the DMPC membrane is observed to be very stable. The structural and dynamical results are in excellent agreement with the X-ray data. The global RMS deviation of the backbone atoms relative to the X-ray structure is 1.4 Å. The side-chains of Ile3, Leu13, Leu43, Trp61, Tyr63, and Phe65, which form a hydrophobic core contributing to the stability of the OmpF trimer, exhibit the smallest fluctuations. Similarly, the strong salt bridges formed by Glu71 (in loop L2) with Arg100 and Arg132 of the neighboring monomer are very stable. The RMS deviations of side chain atoms in the cluster of three positively charged arginines (Arg42, Arg82, and Arg132) are very small, suggesting that a fully charged cluster is consistent with the X-ray structure in agreement with the experimental result of Schirmer & Phale.[15] The size of the pore depends most directly on the structural fluctuations of the PEFGG motif located at the

tip of loop L3 which forms the most flexible region in the narrowest region of the pore. The largest effect on the size of the pore arises from the displacement of Pro116. Other residues, including the arginine cluster and Asp113, are very stable.

The electrostatic potential arising from OmpF has important consequences on the average distribution of ions and water molecules in the aqueous pore. In the narrowest part of the pore forming the "constriction zone", the dipoles of the water molecules are markedly oriented perpendicular to the channel axis because of the strong transversal electrostatic field arising from the arginine cluster and two acidic residues (Asp113 and Glu117) on L3. Furthermore, K$^+$ and Cl$^-$ follow two clearly distinct average pathways extending over 40 Å from the extracellular vestibule to the periplasmic vestibule. In the central region of the pore, the two pathways have a left-handed twist, undergoing a rotation of 180° over a distance of about 20 Å from the extracellular vestibule to the pore periplasmic side. The contributions from water molecules and protein atoms to the solvation of the ions vary in a complementary fashion across the pore in order to keep the total solvation of both ions approximately constant and similar to that in bulk solution. More K$^+$ are found than Cl$^-$ inside the pore in the ion density profile, in accord with the cation selectivity of the channel. In particular, it is observed that the passage of Cl$^-$ occurs only in the presence of K$^+$ counterions, and isolated K$^+$ can move through the channel and permeate on their own. The presence of K$^+$ in the pore screens the negative electrostatic potential arising from OmpF to help the translocation of Cl$^-$ by formation of ion pairs. Inside the channel, the diffusion constant of the ions is reduced by about 50% relative to their value in bulk solution.

The current simulation is meant to provide a realistic representation of OmpF under equilibrium conditions, i.e. symmetric solutions with no transmembrane potential. Although the translocation of few ions across the pore can be observed during the trajectory under these conditions, the chaotic displacement of the ions in the pore does not occur in any particular direction and no net flux is expected under such conditions. To estimate the channel conductance, one must calculate the average current with an applied external transmembrane voltage.[29] However, it seems nearly impossible to obtain statistically meaningful average ionic currents from direct MD simulations at the present time. Even in the case of the rapidly conducting OmpF pore with a high salt concentration, all-atom MD would require prohibitively long calculations. To accurately calculate the conductance of the channel it is necessary to rely on approximations that are computationally less expensive than all-atom MD, e.g. BD simulations[31,32] or Poisson–Nernst–Planck electro-diffusion theory in three dimension (3d-PNP).[71] It is hoped that the atomic details extracted from the current MD simulations will provide a rich source

of information for calibrating and validating future studies based on these approximations.

References

1. Benz, R. & Bauer, K. (1988). Permeation of hydrophilic molecules through the outer membrane of gram-negative bacteria. *Eur. J. Biochem.* **176**, 1–19.
2. Jap, B. & Wallan, P. (1990). Biophysics of the structure and functional of porins. *Q. Rev. Biophys.* **23**, 367–403.
3. Nikaido, H. (1993). Transport across the bacterial outer membrane. *J. Bioenerg. Biomembr.* **25**, 581–589.
4. Weiss, M. & Schulz, G. (1992). Structure of porin refined at 1.8 angstroms resolution. *J. Mol. Biol.* **227**, 493–509.
5. Cowan, S., Schirmer, T., Rummel, G., Steiert, M., Ghosh, R., Pauptit, R. *et al.* (1992). Crystal structures explain functional properties of two *E. coli* porins. *Nature*, **358**, 727–733.
6. Kreusch, A. & Schulz, G. (1994). Refined structure of the porin from *Rhodopseudomonas blastica* comparison with the porin from *Rhodobacter capsulatus*. *J. Mol. Biol.* **243**, 891–905.
7. Schirmer, T., Keller, T., Wang, Y.-F. & Rosenbusch, J. (1995). Structural basis for sugar translocation through maltoporin channels at 3.1 angstroms resolution. *Science*, **267**, 512–514.
8. Dutzler, R., Rummel, G., Alberti, S., Hernandez-Alles, S., Phale, P., Rosenbusch, J. *et al.* (1999). Crystal structure and functional characterization of ompk36, the osmoporin of *Klebsiella pneumoniae*. *Structure*, **7**, 425–434.
9. Buchanan, S. (1999). β-Barrel proteins from bacterial outer membranes: structure, function and refolding. *Curr. Opin. Struct. Biol.* **9**, 455–461.
10. Schulz, G. (1996). General to specific, native to engineered passive pores. *Curr. Opin. Struct. Biol.* **6**, 485–490.
11. Schirmer, T. (1998). General and specific porins from bacterial outer membranes. *J. Struct. Biol.* **121**, 101–109.
12. Koebnik, R., Locher, K. & van Gelder, P. (2000). Structure and function of bacterial outer membranes: barrels in a nutshell. *Mol. Microbiol.* **37**, 239–253.
13. Benz, R., Schmid, A. & Hancock, R. (1985). Ion selectivity of gram-negative bacterial porins. *J. Bacteriol.* **162**, 722–727.
14. Saint, N., Lou, K., Widmer, C., Luckey, M., Schirmer, T. & Rosenbusch, J. (1996). Structural and functional characterization of ompf porin mutants selected for larger pore size II. Functional characterization. *J. Biol. Chem.* **271**, 20676–20680.
15. Schirmer, T. & Phale, P. (1999). Brownian dynamics simulation of ion flow through porin channels. *J. Mol. Biol.* **294**, 1159–1167.
16. Phale, P., Philippsen, A., Widmer, C., Phale, V., Rosenbusch, J. & Schirmer, T. (2001). Role of charged residues at the ompf porin channel constriction probed by mutagenesis and simulation. *Biochemistry*, **40**, 6319–6325.
17. Buehler, L., Kusumoto, S., Zhang, H. & Rosenbusch, J. (1991). Plasticity of *Escherichia coli* porin channels. *J. Biol. Chem.* **266**, 24446–24450.
18. Brunen, M., Engelhardt, H., Schmid, A. & Benz, R. (1991). The major outer membrane protein of *Acidovorax delafieldii* is an anion-selective porin. *J. Bacteriol.* **173**, 4182–4187.
19. Phale, P., Schirmer, T., Prilipov, A., Lou, K., Hardmeyer, A. & Rosenbusch, J. (1997). Voltage gating of *Escherichia coli* porin channels: role of the constriction loop. *Proc. Natl Acad. Sci. USA*, **94**, 6741–6745.
20. Bjorksten, J., Soares, C., Nilsson, O. & Tapia, O. (1994). On the stability and plastic properties of the interior 13 loop in *R. capsulatus* porin—a molecular dynamics study. *Protein Eng.* **7**, 487–493.
21. Soares, C., Bjorksten, J. & Tapia, O. (1995). L3 loop-mediated mechanisms of pore closing in porin—a molecular dynamics perturbation approach. *Protein Eng.* **8**, 5–12.
22. Watanabe, M., Rosenbusch, J., Schirmer, T. & Karplus, M. (1997). Computer simulations of the ompf porin from the outer membrane of *Escherichia coli*. *Biophys. J.* **72**, 2094–2102.
23. Bainbridge, G., Mobasheri, H., Armstrong, G., Lea, E. & Lakey, J. (1998). Voltage-gating of *Escherichia coli* porin: a cystine-scanning mutagenesis study of loop 3. *J. Mol. Biol.* **275**, 171–176.
24. Schabert, F., Henn, C. & Engel, A. (1995). Native *E. coli* OmpF porin surfaces probed by atomic force microscopy. *Science*, **268**, 92–94.
25. Muller, D. & Engel, A. (1999). Voltage and pH-induced channel closure of porin ompf visualized by atomic force microscopy. *J. Mol. Biol.* **285**, 1347–1351.
26. Weiss, M., Abele, U., Weckesser, J., Welte, W., Schiltz, E. & Schulz, G. (1991). Molecular architecture and electrostatic properties of a bacterial porin. *Science*, **254**, 1627–1630.
27. Karshikoff, A., Spassov, V., Cowan, S., Ladenstein, R. & Schirmer, T. (1994). Electrostatic properties of two porin channels from *Escherichia coli*. *J. Mol. Biol.* **240**, 372–384.
28. Brooks, C. III, Karplus, M. & Pettitt, B. (1988). Proteins. A theoretical perspective of dynamics, structure and thermodynamics. In Advances in Chemical Physics (Prigogine, I. & Rice, S. A., eds), vol. 71, Wiley, New York.
29. Suenaga, A., Komeiji, Y., Uebayasi, M., Meguro, T., Saito, M. & Yamato, I. (1998). Computational observation of an ion permeation through a channel protein. *Biosci. Rep.* **18**, 39–47.
30. Tieleman, D. & Berendsen, H. (1998). A molecular dynamics study of the pores formed by *Escherichia coli* ompf porin in a fully hydrated palmitoyloeoyl-phosphatidylcholine bilayer. *Biophys. J.* **74**, 2786–2801.

31. Im, W., Seefeld, S. & Roux, B. (2000). A grand canonical Monte Carlo—Brownian dynamics algorithm for simulating ion channels. *Biophys. J.* **79**, 788–801.

32. Im, W. & Roux, B. (2001). Brownian dynamics simulations of ions channels: a general treatment of electrostatic reaction fields for molecular pores of arbitrary geometry. *J. Chem. Phys.* **115**, 4850–4861.

33. Davis, M., Madura, J., Luty, B. & McCammon, J. (1991). Electrostatic and diffusion of molecules in solution: simulations with the University of Houston Brownian dynamics program. *Comput. Phys. Comm.* **62**, 187–197.

34. Madura, J., Briggs, J., Wade, R., Davis, M., Luty, B., Ilin, A. *et al.* (1995). Electrostatics and diffusion of molecules in solution—simulations with the University of Houston Brownian dynamics program. *Comput. Phys. Comm.* **91**, 57–95.

35. Muller, D., Fotiadis, D., Scheuring, S., Muller, S. & Engel, A. (1999). Electrostatically balanced subnanometer imaging of biological specimens by atomic force microscope. *Biophys. J.* **76**, 1101–1111.

36. Brooks, B., Bruccoleri, R., Olafson, B., States, D., Swaminathan, S. & Karplus, M. (1983). CHARMM: a program for macromolecular energy minimization and dynamics calculations. *J. Comput. Chem.* **4**, 187–217.

37. MacKerell, A. J., Bashford, D., Bellot, M., Dunbrack, R., Evanseck, J., Field, M. *et al.* (1998). All-atom empirical potential for molecular modeling and dynamics studies of proteins. *J. Phys. Chem. B*, **102**, 3586–3616.

38. Schlenkrich, M., Brickmann, J., MacKerell, A. J. & Karplus, M. (1996). An empirical potential energy function for phospholipids: criteria for parameters optimization and applications. In *Biological Membranes. A Molecular Perspective from Computation and Experiement* (Merz, K. & Roux, B., eds), pp. 31–81, Birkhauser, Boston, MA.

39. Jorgensen, W., Chandrasekhar, J., Madura, J., Impey, R. & Klein, M. (1983). Comparison of simple potential functions for simulating liquid water. *J. Chem. Phys.* **79**, 926–935.

40. Beglov, D. & Roux, B. (1994). Finite representation of an infinite bulk system: solvent boundary potential for computer simulations. *J. Chem. Phys.* **100**, 9050–9063.

41. Roux, B. (1996). Valence selectivity of the gramicidin channel: a molecular dynamics free energy perturbation study. *Biophys. J.* **71**, 3177–3185.

42. Gennis, R. (1989). *Biomembranes: Molecular Structure and Functions*, Springer, New York, NY.

43. Zhang, Y., Feller, S., Brooks, B. & Pastor, R. (1995). Computer simulation of liquid/liquid interfaces. I. Theory and application to octane/water. *J. Chem. Phys.* **103**, 10252–10266.

44. Feller, S., Zhang, Y., Pastor, R. & Brooks, B. (1995). Constant pressure molecular dynamics simulation—the Langevin piston method. *J. Chem. Phys.* **103**, 4613–4621.

45. Ryckaert, J., Ciccotti, G. & Berendsen, H. (1977). Numerical integration of the cartesian equation of motions of a system with constraints: molecular dynamics of *n*-alkanes. *J. Comput. Chem.* **23**, 327–341.

46. Essmann, U., Perera, L., Berkowitz, M., Darden, T., Lee, H. & Pedersen, L. (1995). A smooth particle mesh Ewald method. *J. Chem. Phys.* **103**, 8577–8593.

47. Steinbach, P. & Brooks, B. (1994). New spherical-cut-off methods for long-range forces in macromolecular simulation. *J. Comput. Chem.* **15**, 667–683.

48. Ohtaki, H. & Radnai, T. (1993). Structure and dynamics of hydrated ions. *Chem. Rev.* **93**, 1157–1204.

49. Woolf, T. & Roux, B. (1994). Molecular dynamics simulation of the gramicidin channel in a phospholipid bilayer. *Proc. Natl Acad. Sci. USA*, **91**, 11631–11635.

50. Woolf, T. & Roux, B. (1996). Structure, energetics and dynamics of lipid–protein interactions: a molecular dynamics study of the gramicidin A channel in a DMPC bilayer. *Proteins: Struct. Funct. Genet.* **24**, 92–114.

51. Roux, B. & Woolf, T. (1996). Molecular dynamics of pf1 coat protein in a phospholipid bilayer. In *Biological Membranes. A Molecular Perspective from Computation and Experiment* (Merz, K. & Roux, B., eds), pp. 555–587, Birkhauser, Boston, MA.

52. Bernèche, S., Nina, M. & Roux, B. (1998). Molecular dynamics simulation of melittin in a dimyristoyl-phosphatidylcholine bilayer membrane. *Biophys. J.* **75**, 1603–1618.

53. Venable, R., Zhang, Y., Hardy, B. & Pastor, R. (1993). Molecular dynamics simulations of a lipid bilayer and of hexadecane: an investigation of membrane fluidity. *Science*, **262**, 223–226.

54. Bernèche, S. & Roux, B. (2000). Molecular dynamics of the KcsA K + channel in a bilayer membrane. *Biophys. J.* **78**, 2900–2917.

55. Roux, B. (1997). The influence of the membrane potential on the free energy of an intrinsic protein. *Biophys. J.* **73**, 2980–2989.

56. Nina, M., Beglov, D. & Roux, B. (1997). Atomic radii for continuum electrostatics calculations based on molecular dynamics free energy simulations. *J. Phys. Chem. B*, **101**, 5239–5248.

57. Im, W., Beglov, D. & Roux, B. (1998). Continuum solvation model: electrostatic forces from numerical solutions to the Poisson–Boltzmann equation. *Comput. Phys. Comm.* **111**, 59–75.

58. Phale, P., Philippsen, A., Kiefhaber, T., Koebnik, R., Phale, V., Schirmer, T. & Rosenbusch, J. (1998). Stability of trimeric ompf porin: the contributions of the latching loop 12. *Biochemistry*, **37**, 15663–15670.

59. Feller, S., Zhang, Y. & Pastor, R. (1995). Computer simulation of liquid/liquid interfaces. II. Surface tension-area dependence of a bilayer and monolayer. *J. Chem. Phys.* **103**, 10267–10276.

60. Feller, S., Pastor, R., Rojnuckarin, A., Bogusz, S. & Brooks, B. (1996). Effect of electrostatic force truncation on interfacial and transport properties of water. *J. Phys. Chem.* **100**, 17011–17020.

61. Hille, B. (2001). *Ion Channels of Excitable Membranes*, 3rd edit., Sinauer, Sunderland, MA.

62. Goldman, D. (1943). Potential, impedance and rectification in membranes. *J. Gen. Physiol.* **27**, 37–60.

63. Hodgkin, A. & Katz, B. (1949). The effect of sodium ions on the electrical activity of the giant axon of the squid. *J. Physiol.* **108**, 37–77.

64. Lyubartsev, A. & Laaksonen, A. (1996). Concentration effects in aqueous NaCl solutions. A molecular dynamics simulation. *J. Phys. Chem.* **100**, 16410–16418.

65. Degrève, L. & da Silva, F. (1999). Large ionic clusters in concentrated aqueous NaCl solution. *J. Chem. Phys.* **111**, 5150–5156.

66. Roux, B. & Karplus, M. (1991). Ion transport in a gramicidin-like channel: structure and thermodynamics. *Biophys. J.* **59**, 961–981.

67. Roux, B. & Karplus, M. (1991). Ion transport in a gramicidin-like channel: dynamics and mobility. *J. Phys. Chem.* **95**, 4856–4868.
68. Chiu, S., Novotny, J. & Jakobsson, E. (1993). The nature of ion and water barrier crossing in a simulated ion channel. *Biophys. J.* **64**, 98–109.
69. McGill, P. & Schumaker, M. (1996). Boundary conditions for single-ion diffusion. *Biophys. J.* **71**, 1723–1742.
70. Smith, G. & Sansom, M. (1999). Effective diffusion coefficients of K^+ and Cl^- ions in ion channel models. *Biophys. Chem.* **79**, 129–151.
71. Kurnikova, M., Coalson, R., Graf, P. & Nitzan, A. (1999). A lattice relaxation algorithm for three-dimensional Poisson–Nernst–Planck theory with application to ion transport through the gramicidin a channel. *Biophys. J.* **76**, 642–656.
72. Allen, T., Kuyucak, S. & Chung, S. (2000). Molecular dynamics estimates of ion diffusion in model hydrophobic and KcsA potassium channels. *Biophys. Chem.* **86**, 1–14.
73. Einstein, A. (1926). *Investigation on the Theory of Brownian Movement. Translation by A. D. Cowper of papers published 1905–1908*, Dover Publications, New York.
74. Mills, R. & Lobo, V. (1989). *Self-diffusion in Electrolyte Solutions*, Elsevier, Amsterdam.
75. van der Spoel, D., van Maaren, P. & Berendsen, H. (1998). A systematic study of water models for molecular simulation: derivation of water models optimized for use with a reaction field. *J. Chem. Phys.* **108**, 10220–10230.
76. Mahoney, M. & Jorgensen, W. (2001). Diffusion constant of the tip5p model of liquid water. *J. Chem. Phys.* **114**, 363–366.
77. Lee, B. & Richards, F. (1971). The interpretation of protein structures: estimation of static accessibility. *J. Mol. Biol.* **55**, 379–400.
78. Richards, F. (1977). Areas, volumes, packing, and protein structure. *Annu. Rev. Biophys. Bioeng.* **6**, 151–176.

Edited by B. Honig